Dissertation zur Erlangung des
Doktorgrades der Naturwissenschaften (Dr. rer. nat.)
im Fachbereich Geowissenschaften der Freien Universität Berlin

Simulated And Observed Sea Level And Ocean Mass Variations

Julian Kuhlmann

Berlin, Oktober 2013

Institut für Meteorologie
Freie Universität Berlin

GFZ
Helmholtz-Zentrum
POTSDAM

Freie Universität Berlin

1. Gutachter: **Prof. Dr. Maik Thomas**
2. Gutachter: **Prof. Dr. Uwe Ulbrich**

Datum der Disputation: **7. Februar 2014**

Abstract

Mass distribution in the global ocean, equivalently described in terms of Ocean Bottom Pressure (OBP), varies on a broad range of temporal and spatial scales. It can be measured either in-situ or from space with satellites. In-situ measurements are performed either directly with sensors placed on the sea floor or indirectly through the deformation of the Earth's crust. Furthermore, ocean mass distribution can be modeled numerically. This work aims at combining measurements of OBP and sea-surface height with simulations to investigate physical processes which cause temporal and spatial variations of oceanic mass distribution.

Gravitational Self-Attraction and Loading (SAL) of oceanic masses impacts OBP patterns particularly in the case of tides. In order to obtain accurate estimates of tidal amplitudes, frequencies, and phases, the consideration of SAL during the simulation of ocean dynamics is crucial. Additionally, the effects of oceanic, atmospheric, and hydrological loads on non-tidal mass variations have recently moved into the focus of research. These loads evolve more slowly and have smaller amplitudes, thus their importance is less obvious.

In order to simulate the impact of SAL on non-tidal sea level variations, a setup of the global Ocean Model for Circulation and Tides (OMCT) was designed. Modeling results demonstrate SAL to be most important on sub-weekly time scales. Spatially, SAL is particularly important in coastal areas or, due to remote action, in regions where ocean dynamics are weak. Compared to a full consideration of the SAL effect, parameterizations are shown to be inadequate, since their inaccuracies are often of a similar order of magnitude as the impact of SAL itself.

From simulations of ocean dynamics on regional scales carried out with the Regional Ocean Modeling System (ROMS), focussing on the surroundings of South Africa, it emerges that non-tidal OBP variability on time scales of days to months in this region is strongly influenced by mesoscale eddies called Agulhas Rings. Agulhas Rings are not detectable in OBP data from the current Gravity Recovery and Climate Experiment (GRACE) satellites. Their modeled impact on OBP, however, shows high enough amplitudes, low enough frequencies, and large enough spatial extents for them to be detected once the anticipated tenfold increase in accuracy is achieved with data from future satellite gravity missions.

After the end of the current GRACE mission, a gap in the data will open until the scheduled start of a follow-on mission. A method to fill this gap based on complementary in-situ data is presented. Combining spatial patterns of dominant variability with time series of crustal deformations — measured, for instance, with GPS networks — is pursued in order to extend GRACE data of non-tidal ocean loading into the future. The method predicts deformation with a residual error of 0.5 mm or less on all continental surfaces except in the polar regions.

Future prospects for the investigation of OBP variability include model setups assimilating observational data, implementations of additional physical processes into ocean models, and investigations of recurring patterns with clustering methods.

Kurzfassung

Die Verteilung von Wassermassen im globalen Ozean, gleichbedeutend beschrieben als Ozeanbodendruck (Ocean Bottom Pressure, OBP), variiert auf verschiedensten zeitlichen und räumlichen Skalen. Sie kann in situ oder mit Hilfe von Satelliten gemessen werden. In situ-Messungen werden entweder direkt mit auf dem Meeresboden platzierten Sensoren oder indirekt über die Verformung der Erdkruste durchgeführt. Massenverteilungen können zudem numerisch modelliert werden. Ziel dieser Arbeit ist es, Messungen von OBP und Meereshöhe mit numerischen Simulationen zu kombinieren, um physikalische Prozesse zu untersuchen, welche zeitliche und räumliche Variationen von Massenverteilungen im Ozean verursachen.

Gravitative Selbstanziehung und Auflast (Self-Attraction and Loading, SAL) ozeanischer Massen beeinflusst OBP-Muster insbesondere im Fall von Tiden. Um präzise Abschätzungen der Amplituden, Frequenzen und Phasen von Tiden zu erhalten, ist eine Berücksichtigung von SAL während der Simulation der Ozeandynamik unverzichtbar. Darüber hinaus sind in den letzten Jahren vermehrt die Auswirkungen ozeanischer, atmosphärischer und hydrologischer Auflasten auf Massenverteilungen im Ozean in den Fokus der Forschung gerückt. Diese Auflasten variieren langsamer und mit kleineren Amplituden, so dass ihre Bedeutung unklarer ist.

Um den Einfluss von SAL auf gezeitenunabhängige Meeresspiegelmuster zu modellieren, wurde eine Konfiguration des globalen Ozeanmodells Ocean Model for Circulation and Tides (OMCT) entworfen. Die Modellergebnisse zeigen, dass SAL vor allem auf sub-wöchentlichen Zeitskalen bedeutsam ist. Räumlich ist SAL besonders in Küstengebieten oder, aufgrund von Fernwirkungen, in Regionen mit schwacher Ozeandynamik von Bedeutung. Verglichen mit der vollständigen Berechnung des SAL-Effekts erweisen sich Parametrisierungen als unzureichend, da ihre Ungenauigkeiten oft von ähnlicher Größenordnung wie der Einfluss von SAL selbst sind.

Die Modellierung regionaler Ozeandynamik in der Umgebung Südafrikas, durchgeführt mit dem Regional Ocean Modeling System (ROMS), ergibt, dass tägliche bis monatliche gezeitenunabhängige Bodendruckvariabilität stark von mesoskaligen Eddies, den Agulhasringen, beeinflusst wird. Agulhasringe sind in den OBP-Daten der Gravity Recovery and Climate Experiment (GRACE) Satellitenmission nicht detektierbar. Ihr modellierter Einfluss auf OBP zeigt jedoch Amplituden, die hoch genug, Frequenzen, die niedrig genug, und räumliche Ausdehnungen, die groß genug sind, um sie zu detektieren, wenn die angestrebte Verbesserung der Genauigkeit zukünftiger Satelliten-Schwerefeldmissionen um einen Faktor zehn erreicht wird.

Nach dem Ende der aktuellen GRACE-Mission öffnet sich eine Lücke in den Messdaten bis zum Start der geplanten Folgemission. Eine Methode zum Füllen dieser Lücke, basierend auf komplementären in-situ Messungen, wird präsentiert. Dominierende Variabilitätsmuster im Raum lassen sich mit gemessenen Zeitreihen der Krustendeformation, wie sie zum Beispiel GPS-Netze liefern, kombinieren, um die GRACE-Daten gezeitenunabhängiger ozeanischer Auflasten in die Zukunft fortzusetzen. Die Methode sagt Deformationen mit einem Restfehler von 0,5 mm oder weniger auf allen kontinentalen Oberflächen außerhalb der Polarregionen voraus.

Mögliche Erweiterungen der Untersuchung von Bodendruckvariabilität beinhalten die Assimilation von Beobachtungsdaten in Ozeanmodelle, die Implementierung zusätzlicher physikalischer Prozesse und die Untersuchung wiederkehrender Muster mittels Clustering.

Contents

Chapter 1

Introduction

As Charles F. Brooks put it in 1932, "sea level is not level" (Brooks, 1932). It is therefore relatively easy to criticize estimates for global mean sea level rise on this basis, for instance the 26 to 82 cm the Intergovernmental Panel on Climate Change predicted for the end of the 21st century in their most recent assessment report (Alexander et al., 2013). On the other hand, it is relatively hard to come up with a more adequate projection that takes into account spatial variability. The reason lies in sea level being ceaselessly modified by a wide range of geophysical processes acting on various temporal and spatial scales.

These processes range from tides induced by celestial mechanics over differential heating, over freshwater input from the atmosphere, the hydrosphere, and the cryosphere, over wind-induced anomalies, the thermohaline circulation, and over glacial isostatic adjustment resulting in crustal deformation, to the obvious waves, which on their own come in all sizes from a few microns to thousands of kilometers. The importance of understanding and being able to predict sea level, a variable affecting the livelihood of billions of people, stands against the complexity of describing an interwoven system of which often only the surface is observable.

This surface has now been under close, systematic observation for more than a century. Time series of tide gauges, mostly located in port cities of the Northern Hemisphere, date back to the mid-19th century in some cases (Woodworth et al., 2009). Near-global fields of sea surface heights (SSH) at a weekly temporal resolution have been available since the advent of satellite altimetry in the early 1990s (Cazenave, 2010). To obtain this data, the travel time of radar pulses emitted in nadir direction by the satellite and reflected by the sea surface is used to estimate the present SSH. In hindsight, Walter Munk has described the first among these satellites, TOPEX/Poseidon, as "the most successful ocean experiment of all time" (Munk, 2002). The problem remains, however, that SSH is an integral measure of a superposition of processes occurring throughout the water column at the same time.

One way of reducing this complexity is to subdivide the problem. Changes in SSH are commonly separated into steric, i.e. density-induced, and eustatic, i.e. mass-induced changes. The steric part of SSH variability is particularly difficult to measure, since it results from changing temperature and salinity distributions throughout the water column. The Argo project (`http://www.argo.ucsd.edu`) is one attempt to tackle this difficulty by distributing a large number of temperature/salinity profiling floats (3526 devices in July 2013) drifting freely in the ocean. The combined measurements can be used to assemble a global four-dimensional data set of hydrographic variables. Other attempts include model-aided reanalysis of measurement data such as the ECCO project (`http://www.ecco-group.org/`).

Parts of the geodetic community in particular have focused on eustatic SSH variability (e.g. Chambers et al., 2004; Janjić et al., 2012), especially since the launch of the Gravity Recovery and Climate Experiment (GRACE) satellite pair which has been measuring variations of the Earth's gravity field since 2002 and has been used in a number of oceanographic studies (e.g.

Dobslaw and Thomas, 2007; Leuliette and Miller, 2009). While GRACE measures the variability of mass distribution in time, the Gravity Field and Steady-State Ocean Circulation Explorer (GOCE) satellite (Rummel et al., 2011) focuses on the static component of the mass field. This geodetic instrument delivers gradiometric data of unprecedented accuracy that also provides, in combination with altimetric data of the oceans' geometry, information about the constant part of the geostrophic currents. Mass redistributions in the ocean is equivalently described as the variation of ocean bottom pressure (OBP). It can not only be measured by satellite, but also in-situ with bottom pressure recorders which have been deployed on the seafloor in various dynamically interesting parts of the ocean (Quinn and Ponte, 2011). Their lack of spatial coverage as in-situ devices is made up by unequaled precision and temporal resolution.

Shifting water masses in the ocean result in deformation of the Earth's crust. On long timescales, i.e. decades to millennia, and especially when melting ice sheets are considered, a combination of elastic and viscoelastic deformation leads to an adjustment of the Earth's shape to the changed loading (Farrell and Clark, 1976). The result is a delayed rebound of areas where large quantities of ice have depressed the surface, for example after the retreat of the Laurentide and Fennoscandian ice sheets. The resulting change in the shape of ocean basins is especially important for the investigation of relative sea level, i.e. the location of the shore line (Klemann and Wolf, 2007). On shorter timescales, say interannual and below, the viscoelastic contribution can be neglected and the crust behaves purely elastically (Accad and Pekeris, 1978). Crustal deformation also leads to measurable consequences in terms of a modified gravity field, an effect that can even have remote consequences which makes ocean mass variability potentially measurable on land (Kroner et al., 2009).

The goal of this study is to increase understanding of processes leading to spatial variability of sea level changes on time scales from days to a few years. The focus lies specifically on eustatic contributions, i.e. the redistribution of mass, its modeling, and its measurability with geodetic techniques. The first study will be centered on gravitational self-attraction and loading (SAL) of ocean masses, its theoretical description, and its applications in ocean modeling (Chapter 2). A detailed review of the published research in the field will determine in what applications SAL needs to be considered and what approximations are justified. It will also identify gaps in the knowledge about the processes. The next study will address one of these gaps by implementing SAL in a baroclinic ocean circulation model and evaluating the results (Chapter 4). Questions are what magnitude the changes invoked by SAL attain and whether scalar approximations of the process are adequate. Since the ocean model used in this part of the work runs at a relatively coarse resolution while many oceanic processes occur on smaller spatial scales, a different, regional, ocean model will be employed in the next study which will investigate the effect of mesoscale variability on ocean mass variability in the oceans surrounding Southern Africa (Chapter 6). Questions include where and in what intensity SSH and OBP vary in the region and with what sort of measuring devices, in-situ or satellite based, these variations are detectable. One consequence of the described oceanic mass variations is the deformation of the crust. Measurements of this variable are mostly limited to in-situ techniques, so the last study (Chapter 8) will provide a method to estimate the global field of ocean-induced crustal deformation based on measurements at a small number of locations and investigate its accuracy on different timescales.

Chapter 2

Self-Attraction And Loading Of Oceanic Masses

Accepted for publication: Kuhlmann, J., M. Thomas, and H. Schuh, 2013: Self-Attraction and Loading of Oceanic Masses. In *Handbook of Geomathematics*, ed. Freeden, W., M. Zuhair Nashed, and T. Sonar, xx–yy. Vol. 1, Springer Verlag. `http://www.springer.com/mathematics/applications/book/978-3-642-01545-8`.

Abstract. When attempting to simulate sea-level variations precisely, the gravitational potential of the moving water masses themselves and their capability of modifying the Earth's shape have to be considered. Self-Attraction and Loading (SAL) describes said effects. We describe SAL theoretically, deriving equations that allow to compute SAL either with spherical harmonic functions or with a convolution integral, and show how the equations can be modified to reduce computational demands of the calculation. Key questions of past and ongoing research on the topic include: a quantification of SAL at periods from days to years and generated by different processes; the possibility of dynamical feedbacks; and the question of how SAL can be adequately represented in various modeling applications. Gravitation being a body force of infinite range, investigations of SAL include a wide range of processes connected to mass redistribution. For instance, this includes the fast tidal variability, but also atmospherically induced ocean dynamics, or mass redistribution on land and in the atmosphere. Future research is expected to be focused on tidal applications and to consider SAL on longer time scales as an equilibrium response.

Chapter 3

Gaps In The Knowledge About Self-Attraction and Loading

The previous chapter discussed the extensive preceding research on the effects of SAL on modeled tidal sea-level patterns as well as the less extensive research on non-tidal variations. While the simulation of tides requires experiments of relatively short duration since the phenomenon is periodic, the transient non-tidal variations require experiments of longer duration. The computational requirements of an explicit consideration of SAL during the model runs have led ocean modellers to either neglect the effect or to approximate it in the post-processing of their data. The shifting of SAL computations into the post-processing has, however, been employed without a quantitative estimation of the error such an approach brings about.

The following chapter provides such a quantitative estimate. It is based on sensitivity studies with an ocean model that can either simulate SAL or neglect it. The Ocean Model for Circulation and Tides, OMCT, applied here is running at a horizonatal resolution of 1.875° in latitude and longitude, which is coarse enough to make the decomposition into spherical harmonic functions manageable. Especially when a number of sensitivity experiments with varying parameters are performed, it is necessary to keep the computing time for a singel model experiment low.

Furthermore, OMCT has been validated with a particular focus on mass variations. The capabilities of OMCT to reproduce observed ocean currents, SSH patterns, and horizontal transports have been evaluated in Dobslaw (2007). OMCT succeeds in reproducing the basin-wide structures of oceanic gyres, even though the lateral SSH gradients are underestimated in the North Atlantic. Position and strength of the ACC match altimetric observations closely; volume transports through the Drake passage as well as through the Bering Strait are in agreement with in-situ observations. Meanwhile, transports through the Florida Strait are underestimated. Their direct comparison to observations is, however, not possible since the coarse resolution of OMCT lacks islands in this region. Results from OMCT simulations are also used for de-aliasing of GRACE data with respect to SSH and OBP variations occurring on time scales below the GRACE resolution and have been shown to explain about 40% of the corresponding signal mesaured in the most dynamic areas of the ocean, particularly in the Southern Ocean, the North Atlantic, and the North Pacific (Dobslaw et al., 2013).

Besides providing validated runs forced with atmospheric reanalysis data, OMCT has the additional advantage of being a baroclinic ocean model. Variations of SSH and the accompanying horizontal currents are commonly separated into a barotropic and a baroclinic part. In the *barotropic* case, the isobars (surfaces of constant pressure) are parallel to the isopycnals (surfaces of constant density). In this case, horizontal pressure gradients result only from an inclination of the water surface and span the entire water column. They lead to a vertically homogeneous

force from high to low pressure, which is diverted by the Coriolis force. The result is a current of equal velocity throughout the water column.

In the *baroclinic* case, the isobars are tilted with respect to the isopycnals. This can be a result of horizontally adjacent water masses with differences in temperature or salinity, leading to differences in density. Such differences are caused by heat input, evaporation, and freshwater input being spatially heterogeneous. The resulting gradients are steepest in the upper layers of the ocean, where the exchange with the atmosphere occurs. Further below, the water properties vary more slowly with depth. Baroclinic horizontal pressure gradients and the accompanying horizontal motions are therefore strongest in the upper ocean. Furthermore, they induce compensating motions below. At a certain depth, the inhomogeneities above generally cancel out and a level of no motion is reached, where isobars and isopycnals are aligned again. Below this level, the water is at rest and the pressure only varies with depth but is constant in time. Therefore, baroclinic motions often do not leave a trace in OBP, as measured with the GRACE satellites or with Pressure-Inverted Echo Sounders (PIES), while the local variation in density can very well lead to a change in SSH as measured by satellite altimeters or tide gauges.

In numerical ocean models, barotropic conditions are enforced when temperature and salinity are assumed to be constant throughout the ocean. For the simulation of tides, this is often a valid simplification, since forces induced by density differences are negligible in comparison to those induced by the varying gravitational potentials of celestial bodies. Many non-tidal variations, such as El Niño or mesoscale eddies, however, exhibit characteristic temperature and salinity distributions which also influence motions in parts of the water column. It therefore needs to be investigated what impact SAL has on non-tidal SSH variability in a baroclinic ocean model.

A particular area of interest in this context are possible feedbacks. In the assumption of the ocean being an infinitely thin spherical shell, the forces induced by SAL always act on the entire water column. Their relative impact compared to velocities induced by wind, for example, is larger in the abyssal parts of the ocean where velocities are small. The movement of large water masses here can transport large quantities of heat and salt horizontally, thereby modifying the mass distribution throughout the ocean which in turn leads to an SAL effect. The possibility of such feedbacks is a motivation to implement SAL into a baroclinic ocean model at run time.

The OMCT is routinely used in the post-processing of GRACE gravity data in order to correct for short-term variability induced by the atmosphere. In order to be as useful as possible for the task of correting gravity data, a model should contain as many gravity-related processes as possible. Including SAL into OMCT therefore improves the completeness of the model physics.

For routine tasks such as de-aliasing, computational efficiency plays a central role and needs to be balanced with theoretical exactness. A comparison of the complete, theoretically precise formulation of SAL with simple and less time-consuming parameterizations is therefore a task which is relevant, for instance, for the choice of a suitable de-aliasing ocean model for the GRACE post-processing.

Chapter 4

Improved Modeling Of Sea Level Patterns By Incorporating Self-Attraction And Loading

Published as: Kuhlmann, J., H. Dobslaw, and M. Thomas, 2011: Improved modeling of sea level patterns by incorporating self-attraction and loading. *Journal of Geophysical Research*, **116 (C11)**, C11036, doi:10.1029/2011JC007399, `http://dx.doi.org/10.1029/2011JC007399`.

Abstract. We implement the effects of gravitational self-attraction and loading (SAL) into a global baroclinic ocean circulation model and investigate effects on sea-level patterns, ocean circulation, and density distributions. We compute SAL modifications as an additional force on the water masses at every time step by decomposing the field of ocean bottom-pressure anomalies into spherical-harmonic functions and then applying Love numbers to account for the elastic properties of the solid Earth. Considering SAL in the post-processing turns out to be insufficient, especially in coastal waters and on sub-weekly timescales, where SAL modifies local sea level by around 0.6 to 0.8 cm on average; in the open ocean, changes mostly remain around 0.3 cm. Modifications of water velocities as well as of heat and salt distributions are modeled as well, yet they are small. Simple parameterizations of SAL effects currently used in a number of ocean circulation models suffer from the process's inhomogeneity in space and time. These parameterizations improve the modeled sea-level patterns, but fail to reproduce SAL impacts on circulation and density distributions. We therefore suggest to explicitly consider the full SAL effect in ocean circulation models especially when investigating sea-level variations faster than around 4 days.

4.1 Introduction

While global sea level has been rising since the onset of the industrialization (Church and White, 2006; Cazenave et al., 2009), regional sea level shows far more variable patterns on multiple scales in space and time (e.g. Thompson and Demirov, 2006; Wunsch et al., 2007; Oliver and Thompson, 2010). Such patterns are caused by changes in water temperature and salinity, ocean circulation, atmospheric surface pressure, and deformations of the solid Earth and the geoid (Bindoff et al., 2007). Successively, these effects are being implemented into numerical Ocean General Circulation Models (OGCMs). Yet, considerable uncertainties in sea-level projections remain. For instance, the inter-model standard deviation of local secular sea-level trends exceeds the magnitude of those patterns in large parts of the ocean (Meehl et al., 2007; Yin et al., 2010). Improving the representation of those physical effects influencing sea-level patterns in OGCMs is therefore highly relevant for a better simulation of this scientifically and societally crucial variable.

The effects of gravitational self-attraction and loading (SAL), for instance, are either oversimplifyingly parameterized or even outrightly ignored in many OGCMs. The reason for omitting this well-understood effect is the high cost in terms of computing time. SAL has first been described in the early 1970s (Farrell, 1973). Its complete treatment requests either a decomposition into spherical-harmonic functions or a convolution of the field of ocean bottom-pressure anomalies (p'_B) — both ways being equally demanding in terms of computing time. For tidal models, a simple parameterization which goes back to Accad and Pekeris (1978) avoids those kinds of calculations. It consists in simply multiplying the p'_B field by a constant factor. This approach is justified if one spatial scale is dominant in the p'_B field, which was thought to be valid for tides. In view of the rapidly improving accuracy of global geodetic ovservations, Ray (1998) already showed in the late 1990s for tidal models that such a scalar approximation introduces large errors, leading him to the conclusion that "[i]t is difficult to imagine any geodetic application sufficiently precise to warrant ocean-loading corrections and yet sufficiently imprecise to warrant the scalar approximations". Due to the multitude of processes and therefore spatial scales in the general circulation, the prospects of a scalar approximation in OGCMs are even more dire.

On that account, there have been various attempts by ocean modellers to consider SAL in more sophisticated ways: Stepanov and Hughes (2004) implemented SAL with a convolution approach into a barotropic OGCM, focusing on short timescales; Vinogradova et al. (2010); Vinogradova (2011) investigated SAL on monthly and longer timescales, computing the effects as a correction to the model output (a method henceforth called *offline* calculation); and Tamisiea et al. (2010) used the same approach, comparing SAL to similar effects caused by land hydrology and atmospheric loading with a focus on the annual cycle. One limitation of these earlier works is that they fail to allow for dynamic responses of the ocean circulation. An altered ocean circulation may lead to a redistribution of heat and salt which in turn modifies sea-level patterns. This can only be achieved by computing SAL effects during the integration of the OGCM (henceforth called *online* calculation). To our knowledge, we provide the first attempt to run a baroclinic OGCM in a configuration allowing for these effects.

Questions we will answer are: Of what magnitude are SAL effects on relative sea level, ocean circulation, and water density? How useful is an offline calculation of SAL? Does it make sense to treat SAL with a scalar approximation? And how large are our errors if we do so?

4.2 The OMCT Model

The OGCM we use for this study is the Ocean Model for Circulation and Tides (OMCT, Thomas, 2002). The OMCT is a direct descendant of the Hamburg Ocean Primitive Equation Model (Wolff et al., 1996; Drijfhout and Heinze, 1996), but it has been optimized for shorter timescales and can simulate tides as well. It is a serial model based on the nonlinear momentum balance equation, the continuity equation, and conservation equations for heat and salt. The Boussinesq approximation is applied and the total ocean mass is held constant at every time step following Greatbatch (1994). The OMCT in the current configuration has a regular grid of 1.875° resolution in both latitude and longitude. Vertically, the model ocean is discretized at 13 layers whose thicknesses increase with depth but are constant in time. Each model time step is 30 minutes long. The OMCT has first reached a quasi steady-state circulation in a spin-up simulation with climatological wind stresses and mean sea surface temperatures and salinities. Subsequently, it is driven by 6-hourly wind stresses, atmospheric surface pressure, 2m-temperatures, and freshwater fluxes due to precipitation, and evaporation. All of these forcing fields are provided by the ERA-Interim reanalysis project (Dee et al., 2011) of the European Centre for Medium-Range Weather Forecast (ECMWF). Additionally, forcing from continental runoff, excluding ice-sheet contributions, was obtained from the Land Surface Discharge Model (LSDM; Dill, 2008) which is based on ERA-Interim reanalysis data as well. In this study, we analyze 6-hourly output of a simulation in which tidal forcing was deactivated. The study period is the year 2008.

The OMCT has recently been used for investigations of the Earth's rotational parameters (Dobslaw et al., 2010) and routinely helps to de-alias GRACE satellite data (Flechtner, 2007). Quinn and Ponte (2011) showed that the general agreement of OMCT's p'_B signals with in-situ data on timescales shorter than 60 days is relatively weak. Still, in terms of high-frequency p'_B variance, OMCT turned out to come closer to observations than other models, which the authors explained with the inclusion of atmospheric pressure loading in OMCT. In another study, Chambers and Willis (2010) compared monthly p'_B fields from OMCT with altimetric data that they had corrected for steric effects with the help of data from the Argo float network. In this comparison, OMCT achieved high correlations with the observational data almost globally, while some discrepancies appeared in the Southern Ocean.

4.3 Implementation of Self-Attraction and Loading

We derive the magnitude of the combined effects due to self-attraction and loading (SAL) for a baroclinic ocean. The barotropic case has been dealt with by Ray (1998) and Müller (2007).

The Self-Attraction Part The gravitational potential at a location $\mathbf{p}$ induced by a point mass m located at $\mathbf{q}$ in its most general form is

$$V(\mathbf{p}) = \gamma \frac{m}{\overline{\mathbf{pq}}} \tag{4.1}$$

with γ being the gravitational constant. We make the assumption that, since the ocean depth is at least 1000 times smaller than the Earth's radius, we can approximate the ocean as an infinitely thin spherical shell. For such a shell, Equation (4.1) turns into

$$V(\mathbf{p}) = \gamma \iint_S \frac{\sigma(\mathbf{q})}{\overline{\mathbf{pq}}} dS\,. \tag{4.2}$$

Here, $\sigma(\mathbf{q})$ is the surface mass density, i.e. the mass per unit area, at location $\mathbf{q}$ and the integration is carried out over the entire spherical layer. When Ω is the solid angle between $\mathbf{p}$ and $\mathbf{q}$ and R the sphere's radius, the distance between the two points on the sphere is

$$\overline{\mathbf{pq}} = 2R \sin\left(\frac{\Omega}{2}\right) = 2R\sqrt{\frac{1-\cos\Omega}{2}} = R\sqrt{2-2\cos\Omega} \tag{4.3}$$

(Abramowitz and Stegun, 1972, p. 72), which resembles the series of the Legendre Polynomials

$$\sum_{n=0}^{\infty} P_n(\cos\Omega) = \frac{1}{\sqrt{2-2\cos\Omega}} = \frac{R}{\overline{\mathbf{pq}}}\,. \tag{4.4}$$

Now let us insert this into Equation (4.2), considering that since we are on a spherical shell of zero thickness, the surface mass density $\sigma(\mathbf{q})$ is $\sigma(\lambda', \phi')$.

$$V(\mathbf{p}) = \frac{\gamma}{R} \iint_S \sigma(\lambda', \phi') \sum_{n=0}^{\infty} P_n(\cos\Omega) dS \tag{4.5}$$

We know that we can decompose our surface mass density into spherical harmonics as

$$\sigma_n(\lambda, \phi) = \frac{2n+1}{4\pi R^2} \iint_S \sigma(\lambda', \phi') P_n(\cos\Omega) dS\,. \tag{4.6}$$

This holds for a spherical shell of radius R (cf. Smirnow, 1955, p. 427 for a description of the special case R=1). Note that σ_n includes a summation over all orders $m = 0, \ldots, n$, which we omitted here for brevity. Back to Equation (4.5): We exchange the integration and the summation, which we can do since $\sigma(\lambda', \phi')$ does not depend on n, and we then replace the integral with the identical expression from Equation (4.6). This leads us to

$$V(\mathbf{p}) = \gamma 4\pi R \sum_{n=0}^{\infty} \frac{\sigma_n(\lambda, \phi)}{2n+1}\,. \tag{4.7}$$

Rewriting the gravitational constant γ in terms of Earth's gravity g leads us to a new expression for the potential of our spherical shell:

$$V(\mathbf{p}) = \frac{4\pi R^3 g}{M_e} \sum_{n=0}^{\infty} \frac{\sigma_n(\lambda, \phi)}{2n+1}\,. \tag{4.8}$$

We clean up a little by inserting the average density of the Earth $\rho_e = 3M_e/(4\pi R^3)$:

$$V(\mathbf{p}) = \frac{3g}{\rho_e} \sum_{n=0}^{\infty} \frac{\sigma_n(\lambda, \phi)}{2n+1} \,. \tag{4.9}$$

Since we wish to express our surface mass density in terms of bottom pressure anomalies p'_B, we make use of the relation $p = \rho g h$: Our surface mass density σ_n equals volume density ρ times the vertical dimension h, so we replace it with $p'_{B,n}/g$, which leads to

$$V(\mathbf{p}) = \frac{3}{\rho_e} \sum_{n=0}^{\infty} \frac{p'_{B,n}(\lambda, \phi)}{2n+1} \,. \tag{4.10}$$

This is the additional potential on a water parcel at location $\mathbf{p}$ due to gravitational attraction by the anomalous mass distribution on the spherical shell that is described by the spherical harmonics $p'_{B,n}$.

The Loading Part SAL consists of three separate effects, the first of them being the gravitational attraction we just described. What about loading? It leads to the other two SAL effects. On the one hand, the additional mass lowers the seafloor, deforming the Earth elastically; the amount of this displacement is $h'_n V_n/g$, which defines the load Love numbers h'_n. On the other hand, the elastic redistribution of Earth masses in response to the loading shifts the gravitational potential by an amount of $k'_n V_n/g$; again, this defines the load Love numbers k'_n. (Munk and MacDonald, 1960, p. 24). The loading effects are thus proportional to the additional mass, with the proportionality factors reflecting the Solid Earth's properties.

The combination of these three effects that an additional mass exerts — self-attraction, seafloor lowering, and Inner-Earth mass redistribution — requires us to multiply the additional potential from Equation (4.10) with a factor $(1 + k'_n - h'_n)$. This holds for calculations at points fixed relative to the seafloor, thus for a Lagrangian observer (e.g. Blewitt, 2007, p. 385). This Lagrangian point of view is most convenient for us: It saves us from having to redefine the positions of our gridpoints and to manipulate our layer thicknesses at every time step, but it still allows us to consider the dynamical effects of a moving seabed.

The Implementation into the Model The point in our model where we want to implement SAL effects is the computation of horizontal velocities due to pressure gradients, since forces from an additional potential take the same analytical form. The volume force on a water parcel is the negative gradient of the pressure field,

$$\mathbf{F}_{Vol} = -\mathbf{grad}\, p \,. \tag{4.11}$$

We seek to obtain an equivalent formulation for the volume force due to the gravitational potential $\Delta\mathbf{F}_{Vol}$, so we consider that the gradient of the potential is the acceleration, the acceleration times the mass is the force, and the force divided by the volume is the volume force,

$$\Delta\mathbf{F}_{Vol} = \frac{m}{Vol}\, \mathbf{grad}\, V = \rho\, \mathbf{grad}\, V \,. \tag{4.12}$$

Hence, in places where the numerical model calculates volume forces from the pressure field, we can modify the local volume force with the product of the local water density and the gradient of an additional potential. The modified potential in turn is computed from ocean bottom-pressure anomalies with respect to an annual mean field.

We can finally express the modification of local horizontal forces on a water parcel due to SAL as

$$\Delta\mathbf{F}_{Vol} = \rho(\mathbf{p})\,\mathbf{grad}\left(\sum_{n=0}^{\infty}(1+k'_n-h'_n)\alpha'_n p'_{B,n}(\mathbf{p})\right) \qquad (4.13)$$
$$\text{with } \alpha'_n = \frac{3}{\rho_e(2n+1)}\,.$$

For our numerical experiments, we perform three different runs with the OMCT ocean model, hereafter called *Love*, *beta0.1*, and *noSAL*. We use the formulation from Equation (4.14) for the *Love* model run. Herein, we use the *Spherepack 3.2* routine (Adams and Swarztrauber, 2009) for the decomposition of p'_B into spherical harmonics up to degree and order 97, thereby making optimal use of the model's horizontal resolution. We obtained a set of load Love numbers, based on the PREM Earth model (Dziewonski and Anderson, 1981) from `http://gemini.gsfc.nasa.gov/agra/`.

The aforementioned scalar approximation first proposed by Accad and Pekeris (1978) consists in omitting the degree-dependence of the Love numbers. This is justified when the terms of one certain degree dominate the sum of the Stokes coefficients $p'_{B,n}$. Then, Equation (4.14) simplifies to

$$\begin{aligned}\Delta\mathbf{F}_{Vol} &= \rho(\mathbf{p})\,\mathbf{grad}\left(\sum_{n=0}^{\infty}\beta p'_{B,n}(\mathbf{p})\right)\\ &= \rho(\mathbf{p})\beta\,\mathbf{grad}\,p'_B(\mathbf{p})\,,\end{aligned} \qquad (4.14)$$

making the decomposition into spherical harmonics unnecessary. We apply this formulation in the *beta0.1* model run.

For the control run *noSAL*, we set $\Delta\mathbf{F}_{Vol} \equiv 0$, thereby neglecting all SAL effects.

4.4 Results

In order to judge how significant the modifications by appropriately modeled SAL effects on different variables are, we show in Figure 4.1 the standard deviation of differences between the *Love* run and the *noSAL* run, thus the root-mean-square differences between the two runs or, equally, the anomalies caused by SAL. We choose to show these differences for (a) the sea level relative to the ocean floor, (b) the absolute horizontal water velocity in the upper 90 m of the ocean (approximately the mixed layer), and (c) the water density, modified by temperature and salinity, in the same layer. In Figure 4.1, we overlay contour lines that display this standard deviation of differences divided by the standard deviation of the *Love* run alone, i.e. $\sigma(Love - noSAL)/\sigma(Love)$. This quantity is to give an impression of SAL's relative importance. The SAL-induced potential acts identically on water in all depths. In the mixed layer, however,

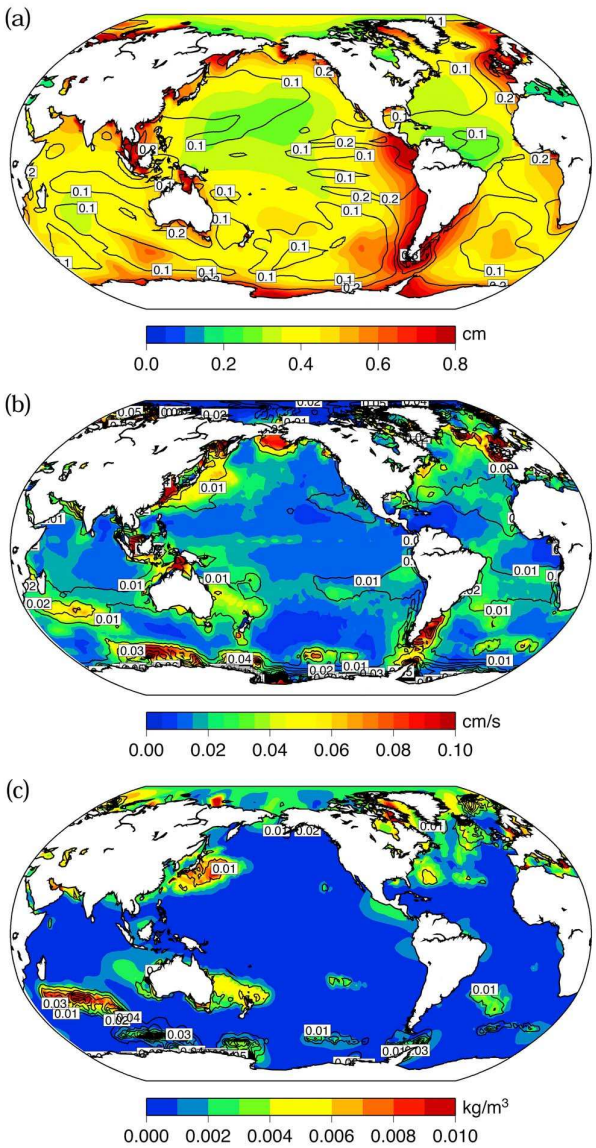

Figure 4.1: Anomalies in (a) relative sea level, (b) absolute horizontal velocity in the upper 90 m, and (c) water density in the upper 90 m caused by SAL effects. Colours show the absolute impact of SAL effects in terms of the standard deviation of differences between the *Love* run and the *noSAL* run. Black contour lines show the relative impact of SAL effects in terms of the former quantity divided by the standard deviation of the *Love* run.

horizontal density gradients are largest, so we expect the most pronounced baroclinic effects here.

Figure 4.1 (a) shows that, in absolute values of sea level, SAL is mostly a coastal effect. Here, strong and varying currents lead to substantial p_B anomalies that induce SAL. Coastal mean deviations commonly reach 0.6 to 0.8 cm, which is equivalent to more than 10% of the simulated sea-level variations in many of those regions. Strong current systems even exert SAL forces on calmer neighbouring regions, as evident in the eastern tropical Pacific, where this leads to mean modifications of the sea level by 20% and more. In the open ocean, deviations mostly remain around 0.3 cm, which translates into around 10%.

In terms of absolute horizontal velocity (Figure 4.1 (b)), SAL is less important. It alters currents by at most 0.1 cm/s, and even this value is only apparent in marginal waters, where simulated velocities are rather inexact due to OMCT's coarse coastline resolution. Horizontal velocities are altered by around 0.05 cm/s in strong current systems such as the Kuroshio, the Gulf Stream, the Antarctic Circumpolar Current (ACC), and the Malvinas Current — where the modifications pale in comparison to the local standard deviations of velocities. The relative SAL impact on mixed-layer velocities therefore mostly remains below 2%.

Changes in ocean currents can lead to changes in the distribution of heat and salt, which in turn can be summarized as density effects. Figure 4.1 (c) shows these effects. In regions of larger velocity modifications, density anomalies are induced, e.g. in the Gulf Stream, the Kuroshio, and north of the ACC along a latitudinal band centered at 30°S. Here, the modifications reach between 0.005 and 0.010 $\mathrm{kg/m^3}$. Except for parts of the southern Indian Ocean, these deviations imply that a dismissal of SAL effects would result in an error of up to 1% only.

Investigations of the evolution of density modifications in time showed that there is no strong trend in the signal: The impact of SAL on sea level is therefore mostly barotropic. This implies that considering SAL at every model time step is mainly important on short timescales. Slow sea-level changes, which are dominated by baroclinic processes, are less affected.

A commmon approach to SAL is the computation of offline corrections to sea-level fields, which for instance Vinogradova et al. (2010); Vinogradova (2011) and Tamisiea et al. (2010) have done for investigations on longer timescales. We check the validity of this approach for our study by correlating the forcing to our SAL routine and the model ocean's response to it. High correlations would indicate a linear response, in which case the offline approach would be sufficient. As forcing term, we take the sum in Equation (4.14), which describes a modification to the local gravitational potential; its gradient acts as a force on the water parcel. As response term, we take the difference in sea level between a run with SAL considered (*Love*) and a run with SAL switched off (*noSAL*). Since the model ocean is expected to take a certain time to adapt to the changed potential, we investigate different time lags between forcing and response fields. Possible time lags are restricted by the 6-hourly time resolution of both fields. The maximum correlation is achieved with a time lag of +6h.

The geographical distribution of these correlations is shown in Figure 4.2 (a). The correlation coefficients are always positive, they vary between 0.2 and 0.8. The lowest values are generally found along the coasts, while high values are achieved in the open ocean, especially in the southern hemisphere and in the Arctic Ocean. As expected, values close to the coasts are lower:

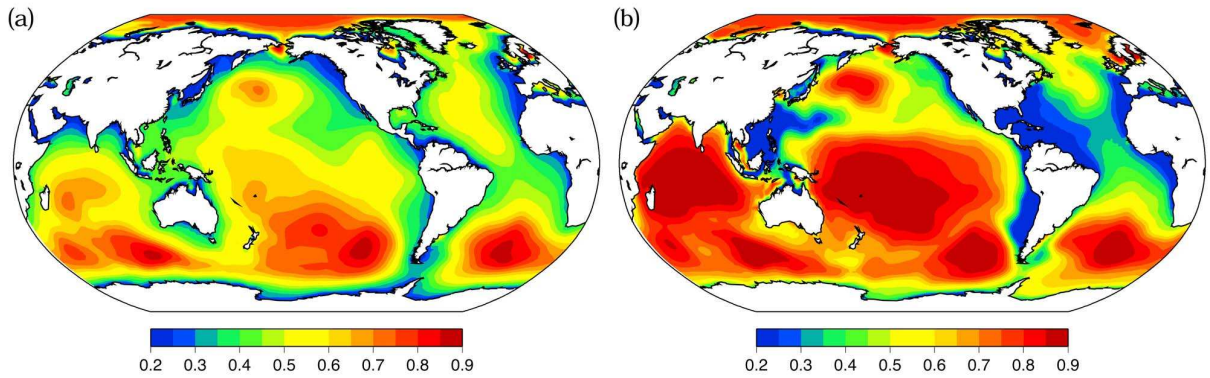

Figure 4.2: Correlations computed along the time axis for every gridpoint of two fields describing the SAL forcing and the response. Forcing: the modification to the local potential due to self-attraction and loading (the sum in Equation (4.14)). Response: the difference in sea level between the *Love* run and the *noSAL* run, thus the anomalous sea level caused by self-attraction and loading. The correlations were computed from 6-hourly data (a) and weekly means (b). In (a), a time lag of +6h is included, supposedly giving the model ocean enough time to adapt to the changed potential. We have tried different lag times between –12h and +12h, the correlations reached a maximum at +6h, which is the field shown here. In (b), we did not apply time lags.

a coast constitutes a horizontal boundary that limits the area from where inflowing water can balance a change in potential. On the other hand, coastal sea level is especially crucial when it comes to predictions for human populations and ecosystems.

If the sea-level response of a model considering SAL is only loosely correlated to the immediate forcing term, then dynamic processes are too important to neglect. The problem of the coastal boundaries is mostly significant on shorter timescales, which justified the offline approach to SAL when longer timescales are considered. However, even when weekly mean values are considered, our model ocean retains large areas with correlation coefficients around 0.6 and below, especially at the coasts, in the North Atlantic, the Equatorial Atlantic, and in the North Pacific (Figure 4.2 (b)). In our OMCT run, p_B variability on timescales longer than one week is especially small in the North Atlantic, which is why correlations remain low in this area. Patterns of correlation similar to those shown in Figure 4.2 (b) are obtained when only variations slower than around 4 days are considered. We hence deduce that, for an adequate representation of SAL effects faster than 4 days, online calculations during the model run are necessary. Slower variations can be sufficiently reproduced by offline corrections.

Nevertheless, even if SAL has to be computed at every time step, there may be ways to reduce the computational complexity. Since the decomposition of the p'_B field into spherical harmonics is computationally expensive, just like the alternative of the field's convolution with the application of Green's Functions, the additional SAL potential term has often been computed as a multiplication of a scalar with the p'_B forcing field. This approach dates back to Accad and Pekeris (1978), who also calculated the value of 0.085 for the scalar factor β in Equation (4.14). A comparable approach, although based on approximating p'_B with the simulated sea-surface heights, has been included in an earlier version of OMCT (Thomas et al., 2001). The magnitude

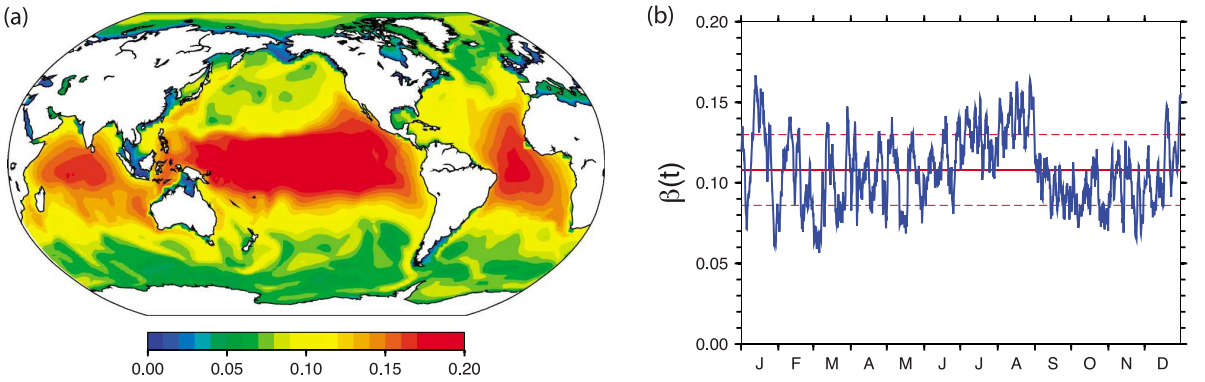

Figure 4.3: Optimal values for β as defined in Equation (4.14) distributed in space and time. For (a), we first described the modifications to the local potential due to self-attraction and loading $V(t)$ (the sum in Equation (4.14)) as a function of the local anomalies in ocean bottom pressure $p'_B(t)$. We then fitted a straight line to this function $V(t) = \beta \cdot p'_B(t) + \text{const.}$. For each gridpoint, β is the slope of this line. The area-weighted mean of the field is $\overline{\beta} = 0.100 \pm 0.072$. The time series in (b) shows $\beta(t)$ as obtained by summing up degree-dependent expression $(1+k'_n-h'_n)\rho\alpha'_n$ from Equation (4.14), weighted by root square sum of the Stokes coefficients calculated from the local anomalies in ocean bottom pressure $p'_B(t)$. The mean value of the time series is $\overline{\beta} = 0.108 \pm 0.022$, as indicated by the red lines.

of β, however, depends very much on the specifications of the ocean model in use. This results from the degree-dependent terms $\alpha'_n(1 + k'_n - h'_n)$ in Equation (4.14), which equal β if summed up. They decrease with increasing degree, thus high variability on smaller spatial scales leads to a smaller β value. The finer the model resolution, the smaller a value for β one would therefore expect, because smaller p_B anomalies can be resolved. We thus refrain from using the Accad and Pekeris (1978) value but compute a β appropriate to our OMCT configuration.

The first way to achieve this is to describe the output of the SAL routine, i.e. the modification of the local potential due to SAL or the parenthesis in Equation (4.14), as a function of the input, i.e. the local anomalies in ocean bottom pressure $p'_B(t)$. The slope of a straight line $V(t) = \beta \cdot p'_B(t) + \text{const.}$ fitted to these points serves as a temporal mean for β at a specific grid point. Its distribution is depicted in Figure 4.3 (a). A clear zonal dependency is obvious: Around the equator, β goes up to 0.2; in the northern and southern extratropics, values around 0.05 prevail. A similar distribution, although achieved with a very different ocean model (OCCAM), has been obtained by Stepanov and Hughes (2004), who argued that smaller p'_B signals in the high latitudes caused by the more complex topography lead to this kind of distribution. The area-weighted mean of the field in Figure 4.3 (a) is $\overline{\beta} = 0.100 \pm 0.072$.

The second way of computing values for β is to take the Stokes coefficients a_{nm} and b_{nm} of the decomposition into orthonormal spherical harmonics that describes the p'_B field at every time step. With a_{nm} and b_{nm}, we quantify the power of the sine and cosine terms of degree n and order m. We compute $\beta(t)$ as the mean value of $\rho\alpha'_n(1 + k'_n - h'_n)$ for all degrees n weighted by the input field's power $\sum_m \sqrt{a_{nm}^2 + b_{nm}^2}$. The result is a value for β at every time step, shown in Figure 4.3 (b). We observe that the mean value $\overline{\beta} = 0.108 \pm 0.022$ is very close to what we obtained from the former way of computation. Furthermore, the spread of $\beta(t)$ around

the mean value is as large as 20%. This, in combination with the large regional variability from Figure 4.3 (a), leads us to be skeptical of transferring the Accad and Pekeris (1978) parameterization, which postulates β to approximately be constant in space and time, from tidal models to circulation models. For tidal models, the Accad and Pekeris (1978) parameterization can be justified by assuming the dominance of one specific spatial scale in the p_B variations. This assumption only fails in regions close to the coast (Ray, 1998). In circulation models, the multitude of spatial scales in p_B variations is apparently inconsistent with the assumption underlying the parameterization.

Lastly, we want to quantify how large the errors are that we make assuming β to be constant anyway. This approach saves us from laboriously decomposing a global field into spherical harmonics and reassembling it at every time step, but instead offers a simple scalar multiplication. In accordance with our results from Figure 4.3, we choose a value of $\beta = 0.1$. We quantify the *beta0.1* run's inaccuracy by first computing its differences to the *Love* run and then taking the standard deviation of these differences (Figure 4.4). To give an impression of the relative importance of these deviations, we also show contour lines describing this inaccuracy as a fraction of the total variability in the *Love* run. Figure 4.4 shows these error measures for (a) the sea level relative to the ocean floor, (b) the absolute horizontal water velocity in the mixed layer, and (c) the water density, modified by temperature and salinity, in the same layer, analogously to Figure 4.1.

In Figure 4.4 (a), we see that the simulated sea level in the parameterized run in the tropical oceans is practically identical to the one computed with the full SAL formulation. In the northern and southern extratropical open oceans, errors are around 0.2 cm; in certain parts of the ACC, they attain 0.4 cm. These errors make out around 5% of the total sea-level signal. Only in certain coastal waters (e.g. Gulf of Thailand, East China Sea, Barents Sea, North Sea), where dynamics are strong and OMCT modeling is arguably weak, errors reach 0.8 cm. Comparing these results with Figure 4.1 (a), we see that the errors in sea level resulting from neglecting SAL can easily be halved by an Accad and Pekeris (1978)-like parameterization.

The picture is different for velocities (Figure 4.4 (b)) and density (Figure 4.4 (c)). Here, errors made by the *beta0.1* run are just as large as if SAL had been omitted in the first place. As explained above, SAL impacts on these two variables are small in absolute values; but if one wishes to consider these impacts anyway, the errors caused by the scalar approximation are too large, reaching up to 0.1 cm/s in velocity and 0.01 kg/m^3 in density. The regional distribution in Figure 4.4 (b) and (c) also shows that there are no regions where a scalar SAL approximation, omitting remote effects, does a particularly good job. As a result, we conclude that a simple parameterization can be of use to improve simulated sea levels, but neither currents nor density distributions.

4.5 Summary

We provide a theoretical description for incorporating the variations of the local potential due to self-attraction and loading (SAL) into a global baroclinic ocean model. After implementing this routine into the OMCT model, we analyzed three one-year simulations: One with SAL

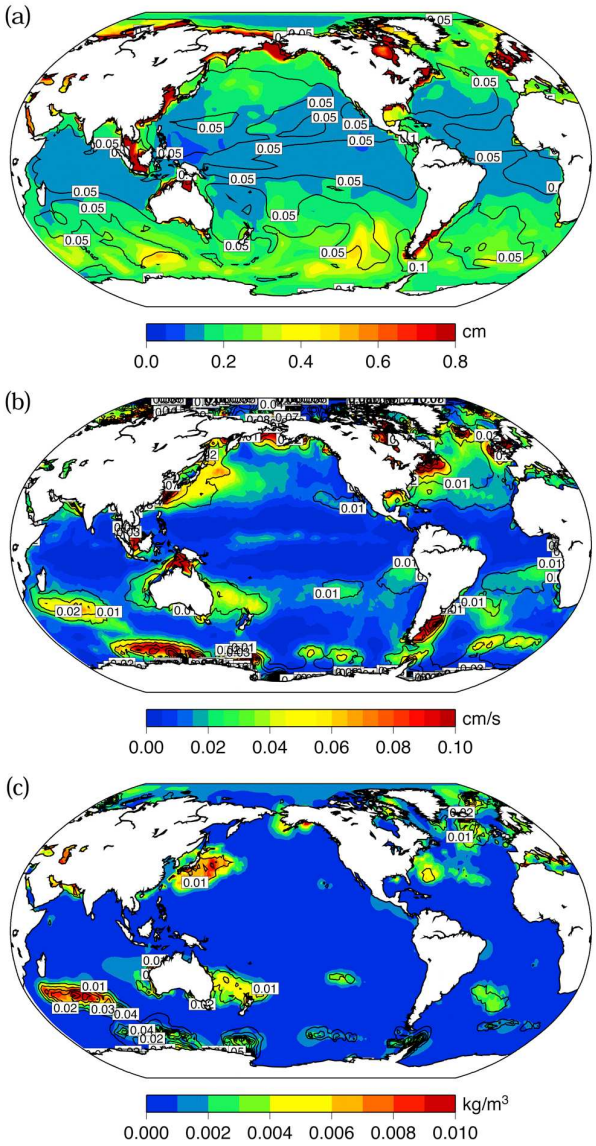

Figure 4.4: Error in (a) relative sea level, (b) absolute horizontal velocity in the upper 90 m, and (c) water density in the upper 90 m caused by using a parameterization instead of the full formulation to describe SAL effects. Colours show the absolute error made in terms of the standard deviation of differences between the *Love* run and the *beta0.1* run. Black contour lines show the relative error caused by the parameterization in terms of the former quantity divided by the standard deviation of the *Love* run.

considered in the theoretically most complete way (*Love*), one with SAL parameterized following Accad and Pekeris (1978) (*beta0.1*), and one with SAL switched off (*noSAL*). We show that, for an accurate representation of SAL, it needs to be calculated during the model run, and not only as a post-processing correction to sea levels. We then go on to show that omitting SAL completely results in errors reaching between 0.6 and 0.8 cm in relative sea level close to the coasts. This is equivalent to a mean error of around 10% in relative sea-level predictions. In the open ocean, these errors mostly remain around 0.3 cm. Feedbacks on horizontal velocities and density are apparent but rather small. Considering a scalar approximation to SAL, as proposed by Accad and Pekeris (1978), we compute an optimal value of the scalar factor β which turns out to be 0.1 for our ocean model. However, large variabilities of β in space and time, as well as the incapability of the parameterization to meaningfully reproduce SAL effects except for the direct effect on sea level, lead us to reject this approach.

4.6 Conclusions

1. A full consideration of SAL effects in a serial baroclinic ocean model is feasible, although the additional computing time at every time step has to be weighed against the expected improvement of the simulations. In the case of OMCT, computing time increases by around 16%.

2. Correcting for SAL in the post-processing seems promising as it saves a lot of computing time. The OMCT, for instance, works with a time step of 30 minutes, while the output fields are only written every 6 hours. However, these post-processing or offline approaches fail to grasp all dynamical feedbacks and all impacts on hydrographic variables. Even for sea level, the possible offline corrections seem doubtful in light of the low correlations between SAL forcing and response we observed on short timescales. For slower variations ($>$ 4 days), offline corrections of sea level are sufficient.

3. Offline corrections are, however, appropriate when timescales are long enough for the ocean to adapt to the new geoid. Since dynamic and baroclinic SAL effects are small, their omission by an offline correction can be justified.

4. SAL is an effect significant enough to be considered in OGCMs if we attempt to make errors smaller than 20% in sea level or smaller than 5% in horizontal velocity and density simulations, at least on sub-weekly timescales.

5. Scalar approximations to SAL are inappropriate since they neglect the strong spatial and temporal variability of bottom-pressure spatial scales, which determine the scalar factor.

4.7 Outlook

What remains to be done until SAL effects are satisfyingly represented in OGCMs? To employ the complete formulation, decomposing the global field of ocean bottom-pressure

anomalies into spherical harmonics at every time step, increases the computing time in the case of OMCT by around 16%; for parallelized models, the price would even be higher. Our implementation of SAL may therefore be useful when the focus lies on high-frequency sea-level variability. When seasonal or interannual timescales are concerned, however, offline corrections are sufficient. The decomposition into spherical harmonics is especially computing-time intensive for models of higher spatial and temporal resolution than OMCT. Therefore, better approximations to the complete formulation, exceeding the scalar approximation in complexity, are desirable. The implementation we came up with can serve as a benchmark for such future approximations. Yet in light of the high frequencies at which nonlinear SAL effects are influential, approximations should not compromise the temporal or spatial resolution of the correcting field. Parameterizations based on latitude, ocean depth, or similar indicators may perform well in some cases (see, for instance, Stepanov and Hughes, 2004), but they lack a sound physical basis that would make them trustworthy without having to test them in each future modeling application.

Another exercise for our model routine, especially once computational efficiency is improved, could be to simulate other sources of high-frequency potential deformation. Examples may be rapid changes in land hydrology or possible interactions between tidal variations and ocean circulation. While in this study we focused on non-tidal ocean loadings, the OMCT also contains an ephemeral tidal model, and our SAL-permitting configuration might be a means to explore this interaction between tides and circulation.

Chapter 5

Intersections Between Global And Regional Scales

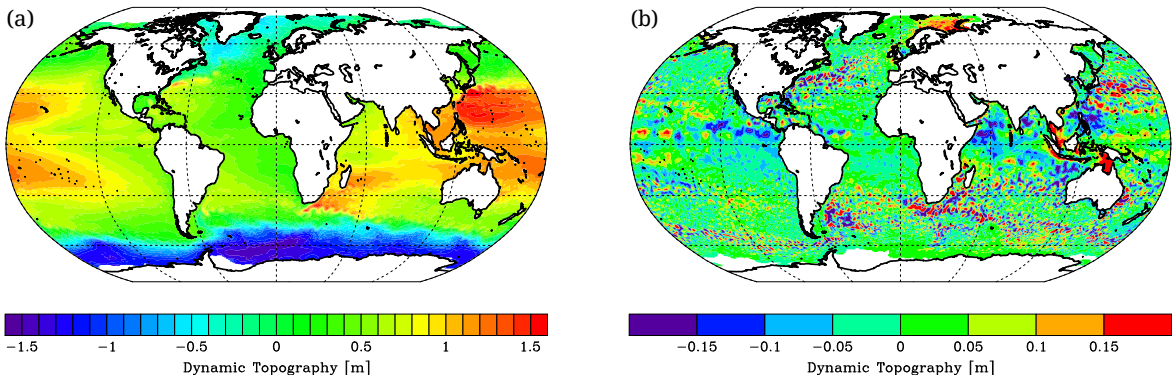

Figure 5.1: Dynamic Topography measured by satellite altimetry as compiled by the AVISO project. (a) The annual mean field for the year 2008. (b) A snapshot of 1 January 2008 from which the annual mean field has been subtracted. Note the different scalings of the color bars.

Global ocean models, such as the OMCT employed in the previous chapter, are an adequate tool for the simulation of large-scale processes such as tides, the meridional overturning circulation, ocean gyres, or the response to atmospheric pressure forcing. They are also adept to simulate a consistent representation of the different ocean basins including exchanges of water masses among them. They are of limited use, however, when mesoscale circulation in a particular region of the ocean is the focus.

The global annual mean field of dynamic topography shown in Figure 5.1a gives a clear picture of the major currents in the world ocean. Gradients in the dynamic topography indicate where the average path of western boundary currents, such as the Gulf Stream, the Kuroshio, or the Agulhas, are located. The path of the ACC and the subtropical gyres emerge from the mean field.

Variations around these mean patterns give a contrasting picture. Figure 5.1b shows the snapshot of one particular day, here 1 January 2008, as an anomaly with respect to the annual mean field from Figure 5.1a. The field of anomalies is dominated by small-scale structures, both positive and negative, often located close to one another. While the anomalies in the Tropics often cover hundreds of kilometers, the diameter of the anomalies in the extratropics decreases to 100 km and less. This is a result of the Coriolis force deflecting currents more strongly at higher latitudes. Meanwhile, the amplitudes of anomalies in dynamically active regions such as the western boundary currents often exceed 0.15 m. Variability of SSH and, linked to it, possibly OBP, on short time scales is thus strongly influenced by mesoscale eddies. Eddies

prevail especially in the western boundary currents where the high velocities in combination with the Coriolis force create turbulent regimes.

The global ocean circulation models discussed in the preceding chapters are discretised at a coarse horizontal resolution on the order of 1 degree. This makes them inadequate for simulations of the highly turbulent dynamical regimes which are active on spatial scales of 1000 km and below and on time scales of days to months. To simulate mesoscale eddies, numerical models of higher horizontal resolution are necessary. In particular, the realistic simulation of turbulence depends more on resolution than on the implementation of SAL described in the preceding chapter. The results showed that SAL effects provide roughly a modification of existing amplitudes on the order of 1 cm. Resolving mesoscale eddies provides additional features of small spatial extent but of large amplitudes — often more than 15 cm, as in Figure 5.1b. While eventually the implementation of SAL would also improve the regional modeling at high spatial resolution, it is not assumed to be central to the appropriate representation of mesoscale eddies.

At a higher horizontal resolution, some parameterizations of subgrid variability may change. The fundamental physics of ocean dynamics however, such as the Navier-Stokes Equation, remain the same. Therefore, the same equations need to be solved on a finer grid. The number of horizontal grid points increases with the square of the horizontal resolution. Additionally, the continuity equation

$$\frac{\partial \rho}{\partial t} + \nabla(\rho \mathbf{v}) = 0 \tag{5.1}$$

links horizontal and vertical motions, making it necessary to increase vertical resolution as well in order to capture turbulences properly. Lastly, dispersion relations connect spatial and temporal scales particularly for phenomena such as Rossby waves, making a higher temporal resolution desirable for models of higher spatial resolution. A tenfold increase in horizontal resolution can therefore easily result in a thousandfold increase in computing time for a numerical ocean model covering the same domain.

The limitations of computing time for scientific experiments with numerical ocean models therefore create a dilemma: One can employ either coarse-resolution models that are incapable of capturing much of the mesoscale variability occurring in the real ocean, or high-resolution models that exhaust the available computational resources before covering time periods that are relevant for climatological processes. This dilemma can be resolved with regional ocean models.

Regional ocean models are employed when, for a specific oceanographic question, only a part of the world ocean is relevant. Boundary conditions provided to the regional model serve as a representation of ocean dynamics beyond this area. Linking the values of variables at the open boundaries of a regional ocean model to the variables of a global model is called *nesting*. In an ocean model, variables considered for nesting are commonly hydrographic variables, such as temperature and salinity, and dynamical variables, such as SSH and momentum. One distinguishes between *one-way nesting* and *two-way nesting*. In the case of one-way nesting, the global model provides the variables at the boundaries to the regional model only In the case of two-way nesting, the output from the regional model is in turn transferred to the global model, allowing for feedbacks outside of the regional model domain. Two-way nesting requires both models to run at the same time, while in the case of one-way nesting the available output

data from a completed run of the global model is used to drive the regional model at a later time.

The results presented in the following chapter come from a one-way nested setup of the Regional Ocean Modeling System (ROMS), driven with output from the global ocean model OMCT. Using the methods of regional ocean modeling, a region of particularly strong small-scale turbulent dynamics, the Agulhas Current off the South African coast and its surroundings, is simulated at a high resolution in order to investigate the impact of mesoscale eddies on SSH and OBP fields.

Chapter 6

Ocean Bottom Pressure Signals Around Southern Africa From In-Situ Measurements, Satellite Data, And Modeling

Published as: Kuhlmann, J., H. Dobslaw, C. Petrick, and M. Thomas, 2013: Ocean Bottom Pressure Signals Around Southern Africa From In-Situ Measurements, Satellite Data, And Modeling. *Journal of Geophysical Research*, **Early View (Online Version of Record published before inclusion in an issue)**, doi:10.1002/jgrc.20372, `http://dx.doi.org/10.1002/jgrc.20372`.

Abstract. Ocean Bottom Pressure (OBP) variability in the region of the Agulhas Current off the South African coast is a crucial variable in the understanding of dynamic processes in the ocean, but measurements currently available lack either precision or spatial and temporal coverage. We provide a quantitative estimate of OBP variability throughout the region with the help of a setup of the ROMS regional ocean model. Driving the model with boundary conditions from a global ocean model and atmospheric reanalysis data and running it for eight years, we are able to reproduce many characteristic properties of the regional ocean circulation visible in sea surface height and OBP fields. While the in-situ pressure inverted echo sounders (PIES) measuring local OBP variations on short time scales are sparse in the region, our model provides a comprehensive estimate of OBP variations throughout the region which reach values of up to 15 hPa when barotropic Agulhas rings reach the Cape Basin. These signals turn out to be difficult to measure with current gravimetry solutions from the GRACE satellites, but estimates of localized noise levels for a GRACE follow-on mission let the search for them in future satellite measurements appear viable.

6.1 Introduction

Global mean sea level rise during the past two decades has been fairly constant at about 3.2 mm/yr (Meyssignac and Cazenave, 2012). Locally, however, the signal varies greatly. The various causes for sea level changes, e.g., heat input from the atmosphere, freshwater input from the cryosphere, river discharge, or changes in ocean currents, leave different regional footprints in the sea level distribution. One way of separating the different physical mechanisms that lead to sea level variability is to distinguish between steric, i.e., density-driven, and eustatic, i.e., mass-driven changes. The vertically integrated density field is measured as Ocean Bottom Pressure (OBP), either by in-situ pressure sensors (e.g., Baker-Yeboah et al., 2010) on the seafloor or by remote sensing devices such as the GRACE satellites (Chambers et al., 2004).

Beyond the attribution of sea level rise to specific causes, better understanding of this variable is also crucial for the understanding of ocean dynamics: variations of barotropic currents leave a signal in the OBP field. Furthermore, the processing of gravitational measurements, either in-situ on land (e.g., Kroner et al., 2009) or with the GRACE satellites (e.g., Dobslaw and Thomas, 2007), depends on high-quality OBP products in order to separate contributions to the gravimetrical signal from different sources such as ice mass changes, hydrology, or crustal deformation. Up to now, those gravimetrical data sets have mostly relied on coarse ocean models in the assumption that mass variations on smaller scales are negligible. With improvements in accuracy of the measurements and reductions of errors from other sources, this assumption may, however, lose its justification.

The high resolution required to resolve small-scale OBP signals makes regional ocean models a powerful tool for flexible investigations. The region we focus on is the surroundings of Southern Africa, dominated by the Agulhas Current and its Retroflection. The Agulhas Current flows from the Mozambique Channel southwards, along the African coast, towards the Cape of Good Hope. At around 34° S, it separates from the coast and continues to flow southwestward (Lutjeharms et al., 1989). When it reaches about 40° S, most of the water masses change direction and are deflected towards the Indian Ocean. At this point, rotating mesoscale structures called Agulhas rings can be either shed into the South Atlantic or change their path and follow the Agulhas Retroflection, which flows parallel to the Antarctic Circumpolar Current (ACC) back eastwards towards the Indian Ocean. The amount of warm and saline water leakage into the Atlantic is still a topic of dispute (van Sebille et al., 2009; Biastoch and Böning, 2013), also due to its possible impacts on global climate (Beal et al., 2011). Since the Agulhas region is rich in mesoscale eddies (Doglioli et al., 2007), it is a prime example for the use of regional numerical ocean models that can run at a higher resolution than their global counterparts. Modeling efforts by Penven et al. (2006) and Rouault et al. (2009) have focused on the immediate surroundings of the Southern African continent. Byrne and McClean (2008) have shown that in a comparison of a high-resolution global model to satellite altimetry data that much of the local variability is not adequately captured by the satellites. In-situ measurement campaigns have attempted to quantify Agulhas Current transport (Bryden et al., 2005), regional tides (Ray and Byrne, 2010), and to track and investigate individual eddy structures (van Aken et al., 2003; Froyland et al.,

2012). Despite increasing research efforts, however, even basic characteristics of the Agulhas Current such as the existence of a seasonal cycle are up for debate (Krug and Tournadre, 2012).

Baker-Yeboah et al. (2009) analyzed local OBP variations in detail using in-situ data from 12 devices measuring a cross section of the eddy corridor through which shedding towards the South Atlantic occurs. They investigated the density structure of the eddies and determined that, in contrast to other eddy-intensive regions in the world such as the Kuroshio, the Agulhas rings often have a strong barotropic component, thus leaving a trace in OBP measurements. In order to determine this mass-induced signal, giving hints about the vertical structure of eddies, altimetric measurements need to be complemented by in-situ or satellite-derived OBP signals.

Our investigations focus on the modeling and observation of OBP in the Agulhas Current region. We will investigate local OBP measurements provided by in-situ Pressure Inverted Echo Sounders (PIES) as well as global OBP measurements with the GRACE satellites. These two data sets show stark disagreements due to the different spatial scales they capture. In order to resolve this conflict and to come up with an estimate of the magnitude and extent of OBP variations throughout the Agulhas region more precise than GRACE data, but at the same time more comprehensive than sparse in-situ measurements, we configure a setup of the regional ocean model ROMS (Shchepetkin and McWilliams, 2005) to simulate mesoscale ocean dynamics around South Africa. After having validated our model setup with satellite altimetry data, we will examine the strongly differing local OBP variabilities measured at the different PIES in the context of our simulation of the dynamics. We will then explore the current technical limitations of GRACE data to detect the Agulhas ring-induced OBP signals the PIES measure and discuss the prospects of satellite gravity data available in the future to capture them.

6.2 Model and Data

6.2.1 Ocean Model

The Regional Ocean Modeling System (ROMS; Shchepetkin and McWilliams, 2005) is a three-dimensional, free-surface, mode-splitting ocean model available free of charge under an open-source license (`http://myroms.org/`). It solves the primitive equations on terrain-following vertical coordinates and has been applied by the scientific community to a wide variety of scenarios ranging from local simulations spanning a few tens of kilometers (e.g., Drews and Han, 2010) up to global simulations (e.g., Song and Colberg, 2011).

Our ROMS setup simulates ocean dynamics in a study area stretching from 57.5° S to 5° S and from 15° W to 55° E (Figure 6.1). Thereby we include, besides the Agulhas Current itself, its confluence from the Mozambique Channel where the Natal pulses originate, the outflow towards the South Atlantic, and a segment of the ACC where in-situ OBP measurements have been taken with PIES (Macrander et al., 2010). The horizontal resolution of the model setup is 0.20° in latitudinal and 0.25° in longitudinal direction. Vertically, we split the water column into 32 layers, their thickness increasing with depth.

Internally, one baroclinic model time step lasts 10 minutes; the barotropic time steps are 15 times shorter. The modeled temperature, salinity, horizontal and vertical velocities, and sea

surface height (SSH) fields are averaged over one day and then stored for later analysis. The spatial distribution of Ocean Bottom Pressure is computed in the post-processing from the 3-D density distribution, the sea level fields, and local depth. We are interested in local rather than domain-wide mass variations, since the latter can be more appropriately modeled with a global ocean model, so we remove variations of the total ocean mass from the data.

Horizontal eddy viscosity is parameterized following Smagorinsky (1963). We chose a value of 0.0125 as the Smagorinsky parameter, thereby producing mesoscale eddies of sizes and magnitudes close to what has been observed by satellite altimetry. A 4th-order Akima scheme deals with horizontal and vertical tracer advection in addition to a generic length scale mixing parameterization (Umlauf and Burchard, 2003).

The boundary conditions at the domain's four open boundaries come from global simulations with the Ocean Model for Circulation and Tides (OMCT; Thomas et al., 2001) run at $1.875° \times 1.875°$, linearly interpolated onto the terrain-following ROMS coordinates with a Matlab toolbox designed by Penven et al. (2008) for that purpose (`http://www.romsagrif.org`). We apply daily mean values of horizontal velocities, temperature, and salinity as well as barotropic momentum and sea surface height. As atmospheric forcing we use 6-hourly wind stresses and net freshwater fluxes from the atmosphere as well as 3-hourly surface heat flux from the ERA-Interim reanalysis (Dee et al., 2011). The same data set has been used to drive the OMCT simulations for the boundary conditions. Information about the local bathymetry comes from the ETOPO2 data set (`http://www.ngdc.noaa.gov/mgg/global/etopo2.html`). Note that the OMCT simulation providing the boundary conditions does not include tides, since the focus of our study is the general circulation only.

The initial fields of temperature and salinity for the model run come, in accordance with the boundary conditions, from OMCT results interpolated on the ROMS grid. Velocities and SSHs start from zero since the different spatial scales of resolved phenomena would make OMCT results rather inadequate for the ROMS grid. We begin the model run on 1 January 2001, and let the model run for two years, forced by atmospheric and oceanic boundary data, as a spin-up. These first two years are not analysed further. Even though large-scale circulation adapts to the T and S initialization fields within days, these two years are needed to produce mesoscale circulation, since meander modes originating from the Mozambique Channel and Agulhas rings spawned from the retroflection south of Cape Town need several months to travel through the region. We then extend the model run by six years which we analyse. Our study period therefore comprises the years 2003 through 2008.

6.2.2 Observational Data

In order to ground our analysis in measurements of the magnitudes in question, we make benefit from the work done by the Archiving Validation and Interpretation of Satellite Data in Oceanography (AVISO) project (`http://www.aviso.oceanobs.com/duacs`). In the AVISO data, satellite altimetry observations from various instruments and platforms are gathered into a single data set, providing a continuous record of daily global sea level fields at $1/3°$ horizontal resolution. Although the data we use is provided on daily fields, the repeat cycles of the satellite

tracks prohibit the extraction of meaningful signals on time scales smaller than a week. AVISO data exist from 1992 up to today.

Satellite data of OBP comes from the Gravity Recovery and Climate Experiment (GRACE). The satellite pair uses inter-satellite distance to estimate the gravitational effect of mass redistribution within the Earth system. We use the ITG-Kalman solutions provided by the Institut für Theoretische Geodäsie, University of Bonn (Kurtenbach et al., 2009). The ITG-Kalman data are based on a Kalman Smoother approach in order to come up with daily fields of mass variations in form of spherical harmonics up to degree and order 40, corresponding to a horizontal resolution of approximately 500 km. Model-based estimates for continental, atmospheric, and solid Earth contributions have been subtracted from the initial data, so we retain a purely oceanographic signal. The ITG-Kalman data are available from August 2002 on.

OBP is further measured by PIES, in-situ devices placed on the seafloor by Alfred-Wegener Institute (Macrander et al., 2010), Proudman Oceanographic Laboratory (Rietbroek et al., 2006), and Centre National d'Etudes Spatiales (see `http://www.psmsl.org/links/programmes/acclaim.info.php`). These PIES, located at twelve positions in or around our model domain, record OBP variations at a temporal resolution of 30 minutes. We have detrended the data in order to account for the sensor drift common to these instruments, removed the tidal signals with a Doodson X0 filter and then computed daily averages of the signal. The length of the time series varies from device to device, reaching from one year to three years. The PIES measurements are therefore most suited for the investigation of signals on annual or shorter time scales. Locations and time periods for which data is available can be found in Table 6.1.

Table 6.1: In-situ OBP measurements collected by AWI Bremerhaven. In the last column, n is the number of days with OBP measurements that were evaluated. Except for *CNES CRO*, each PIES delivered data for more than 98% of the deployment time.

PIES ID	Latitude	Longitude	Start Date	End Date	n
AWI ANT3	37.09° S	12.77° E	7 March 2007	8 February 2008	339
AWI ANT5	41.13° S	9.94° E	29 January 2005	9 February 2008	1107
AWI ANT537	41.18° S	4.26° E	30 August 2006	8 February 2008	528
AWI ANT7-1	44.66° S	7.08° E	29 November 2002	26 January 2005	790
AWI ANT7-2	44.66° S	7.08° E	29 January 2005	11 February 2008	1109
AWI ANT9	47.66° S	4.26° E	1 February 2005	13 February 2008	1108
AWI ANT10	49.01° S	2.83° E	14 December 2006	29 December 2007	381
AWI ANT11	50.26° S	1.43° E	1 December 2002	30 January 2005	792
AWI ANT13a	52.51° S	1.40° W	26 October 2006	17 February 2008	480
CNES CRO	46.55° S	51.79° E	24 January 2002	9 December 2004	1051
POL IO1	47.12° S	54.90° E	25 January 2004	15 February 2005	388
POL IO2	48.83° S	61.28° E	26 January 2004	29 January 2005	370

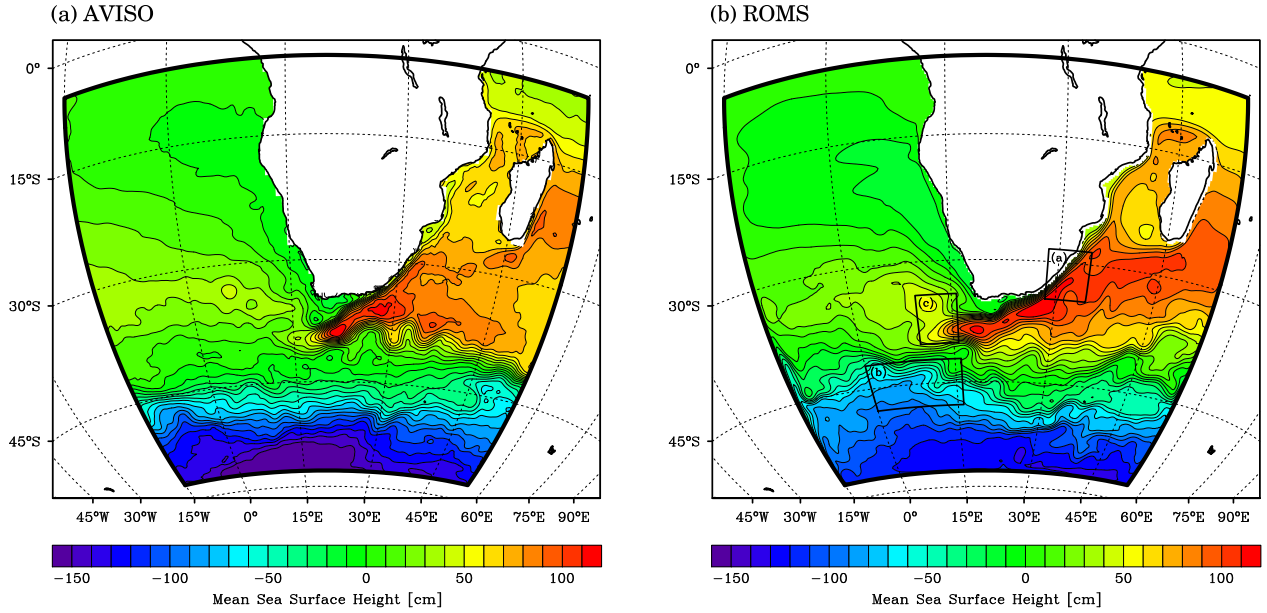

Figure 6.1: Mean detrended Sea Surface Height during the time period of 2003 through 2008, (a) in the AVISO satellite altimetry data, (b) in our configuration of the ROMS model. Both data sets have been brought to a similar spatial average value in order to make them comparable. The black boxes in (b) indicate the areas investigated further in Figure 6.3.

6.3 Results

6.3.1 Initial Model Evaluation

We evaluate the model setup by comparing its output with a well-established satellite altimetry data set. Satellite altimetry, measuring the elevation of the sea surface, has been available for two decades and has been widely applied to describe ocean dynamics, also in the region of this study (Krug and Tournadre, 2012; Byrne and McClean, 2008). We therefore expect that, once the model reliably reproduces patterns of sea level distributions and their variability as integral measures of ocean dynamics, it is also trustworthy in simulating variables linked to ocean dynamics that evade direct measurement. Since a direct comparison of time series is not expected to yield meaningful results in the case of a non-assimilative model setup, we limit our comparisons to statistical quantities.

The mean SSH measured by AVISO (Figure 6.1a) is reproduced by the mean SSH simulated by our ROMS setup (Figure 6.1b) in the crucial, large-scale features of the regional ocean dynamics: The SSH gradients show an Agulhas current of realistic strength, position and extent; an ACC spanning the width of the region and following a path similar to what is observed, although somewhat less zonal; a retroflection transporting most of the Agulhas waters back towards the Indian Ocean; and a region of ring shedding in the South Atlantic. The features are generally more washed out than they are even in a six-year mean of the observations, which nevertheless has to be expected when using a model of 0.25° resolution. There is a discontinuity between the ACC inflow at the western boundary between 35° S and 55° S in the

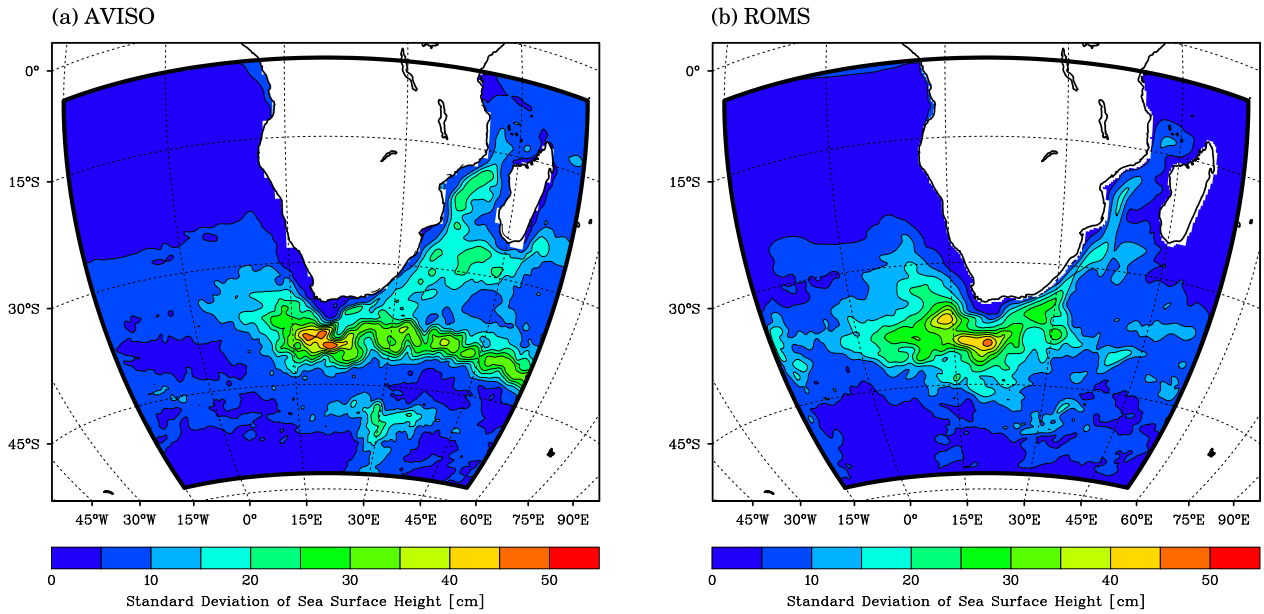

Figure 6.2: Standard deviation of detrended Sea Surface Height weekly means during the time period of 2003 through 2008, (a) in the AVISO satellite altimetry data, (b) in our configuration of the ROMS model.

OMCT boundary conditions and the interior ACC simulation. Since the atmospheric forcing is the same, this must be a result of interior dynamics, presumably due to the different spatial scales resolved. It could also be that different implementations of vertical momentum transport lead to a less vigorous ACC in the global OMCT model. Fortunately, the modeled ACC picks up speed quickly after having entered the model domain, so the boundary artifacts influence only a small area. Outside of this specific section of the western boundary, the transitions from boundary data to interior data are fairly smooth.

Since we aim at reproducing the variations of ocean currents in time, the modeled SSH standard deviation field needs to be close to what has been measured as well. While the model output comes in daily average fields, the effective temporal resolution of the AVISO satellite data is weekly, so we first filter the model output in time to make both data sets comparable. Examining the two fields in Figures 6.2a and 6.2b, we can identify a region of maximum variability in the eastern Cape Basin, where SSH standard deviation reaches values of up to 50 cm. This is the area of strong eddy activity mostly originating from Agulhas ring shedding which has been dubbed "Cape Cauldron" due to the vigorous mixing (Boebel et al., 2003). The surrounding area of increased turbulence comprises parts of the South Atlantic which are slightly more vast in the simulation than in the observations. Also, in the model, the increased variability reaches more westward, while the observations show more of a north-westward extension of this zone, hinting at a difference in the path of outgoing Agulhas rings. The variability within the Agulhas Current, from the Mozambique Channel southward to the Cape region, is very similar in model and observation. A stark difference is apparent along the 40° S latitude band, where retroflected eddies and current meandering lead to a standard deviation in the observations of around 30 cm, while the Return Current in the model is less

turbulent with a standard deviation of only 10 cm. Since our focus in this study lies on the central and western part of the study region, this deficiency can however be tolerated. Furthermore, the comparison of mean SSH fields showed that at least the mean slope of the Agulhas Return Current in the model is reasonable, so reduced variability here should not be detrimental to investigations upstream.

Similar standard deviations can, however, result from variability in very different frequency bands. To investigate whether this is the case, in Figure 6.3 we show spectra of SSH variability in three representative areas indicated in Figure 6.1b: (a) within the Agulhas Current (31.5±3°S, 31.5±3°E), (b) along a part of the ACC (45±3°S, 8±12°E), and (c) around one of the in-situ measurements that will be analysed later (37±3°S, 12.75±3°E). In both the Agulhas Current and the ACC, the model reproduces the dominant seasonal signal apparent in the satellite data. In the Agulhas Current (Figure 6.3a), also a semiannual signal with an amplitude of 20 cm and peaks at shorter periods are correctly captured by the model. On interannual periods, however, the model shows more variability than the satellite data. Meanwhile, on periods of a month and less, the variability the model produces cannot be captured by the satellites due to their slow repeat cycle. This observation is similar to the the conclusions of Byrne and McClean (2008) for the Agulhas region and is also apparent in the data from the ACC section (Figure 6.3b), where the model shows signals on periods below 30 days that are not measured by the satellites. Interannual variability is captured well here with both spectra flattening out at 30 cm. Off the Cape of Good Hope (Figure 6.3c), the model slightly overestimates the variability on sub-monthly time scales while underestimating it on periods of a year and more. On periods between a month and a year, spectra of model and observation mostly do not differ significantly, even though specific features such as the weak annual peak in the observations cannot be reproduced unambiguously. The narrow confidence interval for the ROMS spectrum in Figure 6.3c originates from the shorter temporal autocorrelation length due to the model producing Agulhas rings rather regularly at periods between 1 and 4 months (0.08 and 0.33 yr), which is visible as elevated spectral density. Meanwhile, ring shedding in the observations is more chaotic and occurs on a wider range of periods. Overall, the spectral comparison of observational and model data shows good agreement, providing hints that the most important underlying physical processes are simulated properly in the model.

6.3.2 OBP Signals in Observations and Model

Figure 6.4a shows the standard deviations of daily OBP fields measured by the GRACE satellites (filled contours) and by in-situ PIES (filled circles). These two measurement systems, although tracking the same variable, represent opposing extremes in spatial scales: The GRACE data has a nominal spatial resolution of roughly 500 km. Standard GRACE products provide a temporal resolution of ten days to a month, and great efforts, including the application of a Kalman Smoother, had to be made to come up with global daily fields in the ITG-Kalman solution (Kurtenbach et al., 2009). The decorrelation scales in space and time for the process model of the Kalman Smoother have been taken from the OMCT ocean model. Meanwhile, the PIES are indicative of OBP variations at a very specific location each and deliver data every thirty

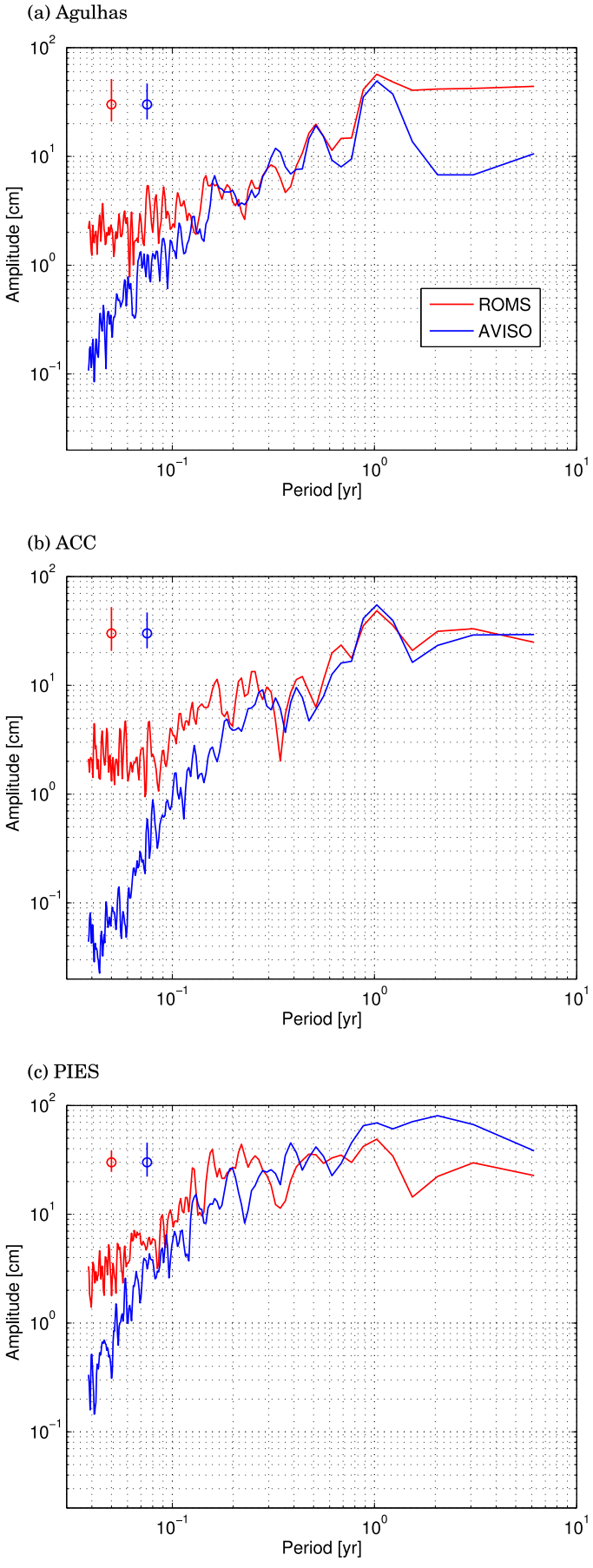

Figure 6.3: Spectra of sea surface heights in the ROMS model and in AVISO satellite data at the three different locations indicated in Figure 6.1b: (a) in the Agulhas Current (31.5±3°S, 31.5±3°E), (b) in the ACC (45±3°S, 8±12°E), (c) around one of the in-situ OBP measurement sites (37±3°S, 12.75±3°E). In the upper left, the 99% confidence levels for each spectrum are indicated.

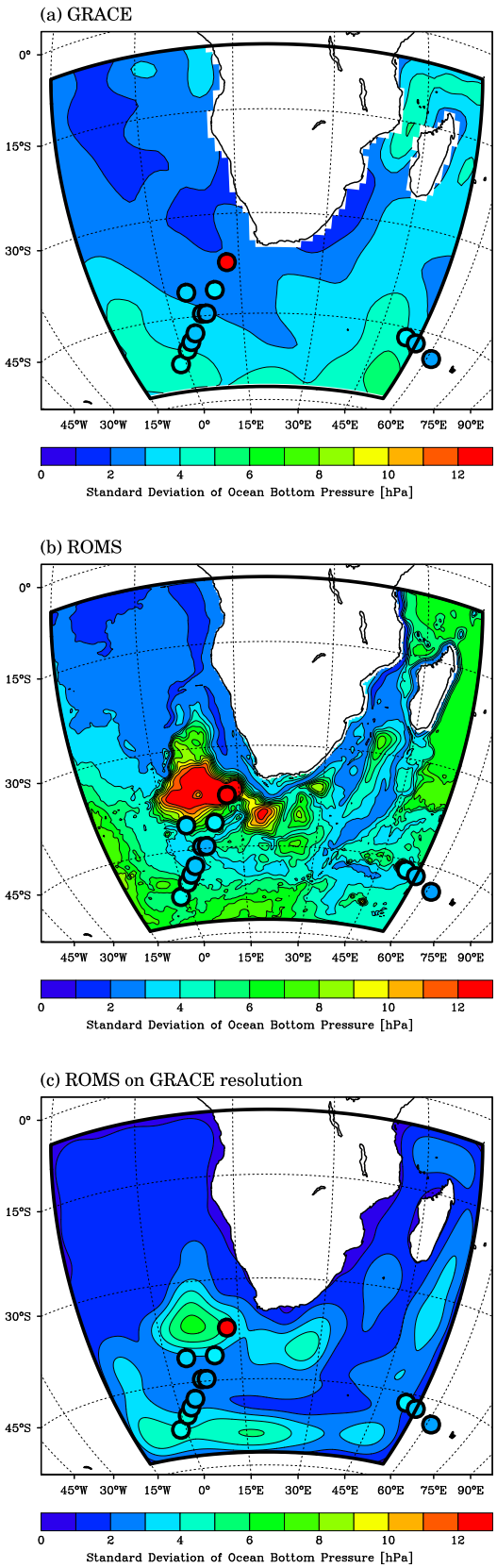

Figure 6.4: Standard deviation of daily Ocean Bottom Pressure fields during the time period of 2003 through 2008, (a) in the ITG-Kalman solution, (b) in our configuration of the ROMS model, (c) in our configuration of the ROMS model with a cutoff at spherical harmonics degree and order 40 and as 10-day means. The filled dots show the standard deviations measured by in-situ PIES.

minutes; the standard deviations in Figure 6.4a originate from data from which the tides were removed with a Doodson X0 filter (Doodson and Warburg, 1941) before daily averages were computed. That said, the comparison shows certain common features. In the GRACE data, apart from stronger variability in the Indian Ocean, a north-south gradient going from an OBP standard deviation of below 3 hPa in the Tropical Atlantic to around 5 hPa south of 45°S is the dominant feature. This gradient is somewhat found again in the PIES data southwest of South Africa, at least in the signals from the devices "AWI ANT7-1" through "AWI ANT13a". There is but one notable exception from this pattern: The in-situ device "AWI ANT3" at 37.09°S, 12.77°E, measuring an OBP variability of 12.5 hPa. This stands out in comparison to both the GRACE data and the other PIES, which all remain around 3 to 4 hPa. It is in agreement, however, with the data presented by Baker-Yeboah et al. (2009) for an earlier time period.

Replacing the GRACE OBP with the modeled OBP standard deviations (Figure 6.4b), it is apparent that certain broad-scale features are well reproduced: The north-south gradient in the Atlantic, as well as increased variability in the Indian Ocean, that GRACE observes are visible in the model simulations. In both cases, the agreements need to be interpreted with caution, since boundary effects might also play a role in their formation. In the case of the Indian Ocean, unfortunately, the lack of PIES leaves us in the dark about whether boundary effects in the simulations, leakage effects in the GRACE data, or physically meaningful ocean variations dominate the variability there. This cannot be said about the strong OBP variability throughout the Cape Basin in the model simulations (between 0° and 15°E, 25°S and 40°S). Here, the ROMS setup produces OBP variability up to 15 hPa, compared to roughly 2.5 hPa in the GRACE data. This area is precisely where the PIES "AWI ANT3" mentioned above is situated, leading us to place confidence in the simulated strong variabilities. The barotropic nature of many Agulhas rings in the Cape Basin has been repeatedly reported in the literature. For example, van Aken et al. (2003) investigated a particular Agulhas ring during a cruise in the year 2000 and showed it to produce currents down to the seafloor. While focussing on a later stage of the lifetime of Agulhas rings, van Sebille et al. (2012) investigated the dynamics involved in great detail.

The ITG-Kalman solution has a horizontal resolution of roughly 500 km, and while it delivers daily average fields, the repeat cycle of the GRACE satellites is much slower, leading to standard GRACE products being delivered only as 10-day mean fields. In order to make the model output more comparable to the GRACE data, we developed it in spherical harmonic functions, set all coefficients beyond degree and order 40 equal to zero, re-synthesized them into the spatial domain, and computed 10-day mean fields. The standard deviation of this mockup satellite data is shown in Figure 6.4c. Compared to Figure 6.4b, the east-west and north-south gradients are dampened but still visible, even though the spatial smoothing of the fields produces artificially low variability at the edges of the study domain. The amplitudes of around 5 hPa in the Southern and Indian Oceans are close to what is observed by GRACE in Figure 6.4a. The high OBP variability in the Cape Basin, however, withstands the smoothing. Its amplitude decreases to around 7 hPa (compared to 15 hPa before the smoothing) but is still the dominant signal in the model output. It is therefore probably not purely due to limited temporal and spatial resolution of the GRACE data that the Agulhas rings are not detected.

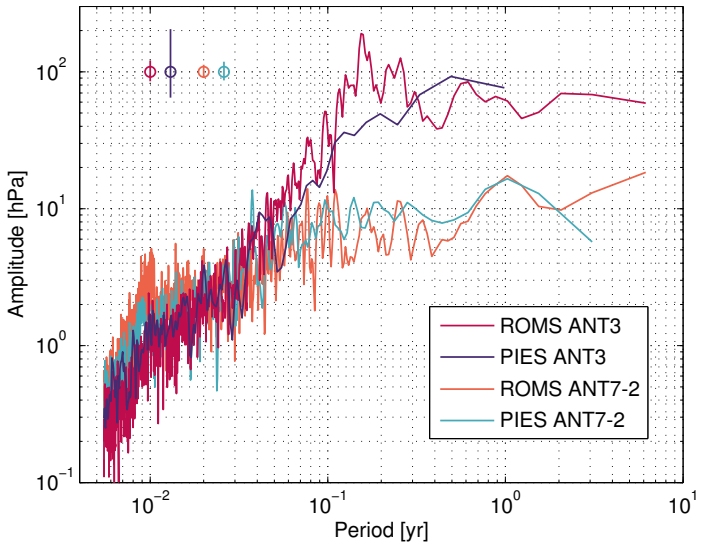

Figure 6.5: Spectra of OBP time series measured by the PIES ANT3 and ANT7-2 (see Table 6.1) compared to the ROMS simulations of OBP at the same locations. In the upper left, the 99% confidence levels for each spectrum is indicated.

In order to judge whether the model simulations of OBP variability agree with the PIES measurements not only in standard deviation, but also in spectral content at different periods, we show the spectra of the signals in Figure 6.5 for two of the measurement locations, ANT3 and ANT7-2 (see Table 6.1). Beside the general redness of the spectra, it is also apparent that the model succeeds in simulating the similar variability at periods from days to about a month and the almost tenfold predominance of the amplitude at periods longer than one month at the site ANT3 compared to ANT7-2. The annual signal at the location of ANT7-2 is accurately simulated by ROMS. Such a signal is absent from the simulation at ANT3 and cannot be detected from the short PIES time series here, which also leads to the broad confidence interval for this spectrum. At periods between 1 and 4 months (0.08 and 0.33 years), the modeled spectrum deviates from the measurements. The peaks here are related to the formation of barotropic Agulhas rings in the model. Too regular ring formation is a shortcoming that many numerical ocean models of the region share (Lutjeharms and Webb, 1995; Backeberg et al., 2009). Nevertheless, the frequency of ring formation is, with about five rings shed per year, in accordance with estimates from the literature (van Aken et al., 2003). The decent overall correspondence in a statistical sense throughout much of the spectrum and also at short periods leads us to believe that the model simulates the local processes governing OBP variability reasonably well and is therefore capable to provide useful quantitative estimates of OBP variability also at locations where no in-situ measurements are available.

6.3.3 Detectability of Agulhas ring-induced OBP signals with GRACE

Consistently with the published literature (Byrne and McClean, 2008; Baker-Yeboah et al., 2009), our model simulations show an OBP signal above 10 hPa of standard deviation caused by Agulhas rings in the Cape Basin. The signal is simulated to spread throughout the basin in

a way that, considering temporal and spatial resolution, it should be detected by GRACE. The ITG-Kalman data, however, shows otherwise.

There are various possible causes for the discrepancy between model and in-situ data on the one hand and satellite data on the other hand. First, the GRACE satellites measure a gravitational signal of both the continental hydrology and ocean mass variations, with the hydrological signal being about three times as strong as the oceanic signal. While the ITG-Kalman solution we use is a pure ocean product, thus attempts have been made to remove the hydrological signal from the data, the proximity of the Cape Basin to the South African coast (about 600 km) could lead to a loss of signal due to exaggerated removal of meaningful ocean mass signal in the GRACE post-processing. Furthermore, the distribution of the GRACE satellite tracks can lead to redundant data at some points and an undersampling of the signal at others. Another culprit may be the background ocean model OMCT whose covariance matrix was used for the Kalman Smoother approach producing the ITG-Kalman solutions. Since Agulhas rings are not present in the OMCT simulations, it is likely that ITG-Kalman underestimates them, too.

Many errors of the GRACE data, however, are well known and quantified. Noise levels for GRACE products are commonly given as a function of spatial scale in terms of the degree of spherical harmonic functions. These noise levels can be compared to the expected signal from a certain geophysical process. A signal-to-noise ratio (SNR) of more than 1 is needed to detect a signal in principle, althouth generally an SNR higher than that will be necessary to measure a signal reliably.

In the case of the highly localized bottom pressure signals we are interested in, additional effort has to be put into the estimation of the SNR. Wieczorek and Simons (2005) and Han and Ditmar (2007) showed how the spherical harmonics spectrum of a signal can be localized by applying a window function to both the signal and the error fields. The window function is chosen in a way that the signal is present in the window only, while the error, by its nature, spans the entire globe. Therefore, the localization can increase the SNR above the threshold of detectability. We follow the same approach and show localized signal and error functions in Figure 6.6a as well as the resulting SNRs in Figure 6.6b. Since GRACE data is commonly distributed in terms of spherical harmonics describing the time-variable gravitational potential that can be displayed as changes in geoid height, the OBP fields need to be transformed into this quantity, too. This is done by first developing the field of surface mass density in spherical harmonic functions and then applying the relation

$$\begin{Bmatrix} C_{lm} \\ S_{lm} \end{Bmatrix} = \frac{3\rho_w}{\rho_{\text{ave}}} \frac{1+k_l}{2l+1} \begin{Bmatrix} \hat{C}_{lm} \\ \hat{S}_{lm} \end{Bmatrix} \tag{6.1}$$

from Wahr et al. (1998) to transform the coefficients of surface mass density $\hat{C}_{lm}$ and $\hat{S}_{lm}$ of degree l and order m into the geoid coefficients C_{lm} and S_{lm} using the density of sea water ρ_w, the average density of the Earth ρ_{ave}, and the degree-dependent load Love numbers k_l (see Farrell, 1972). This transformation leads to the degree variances of the signal decreasing with increasing spherical harmonics degree l. GRACE noise levels, on the other hand, increase with

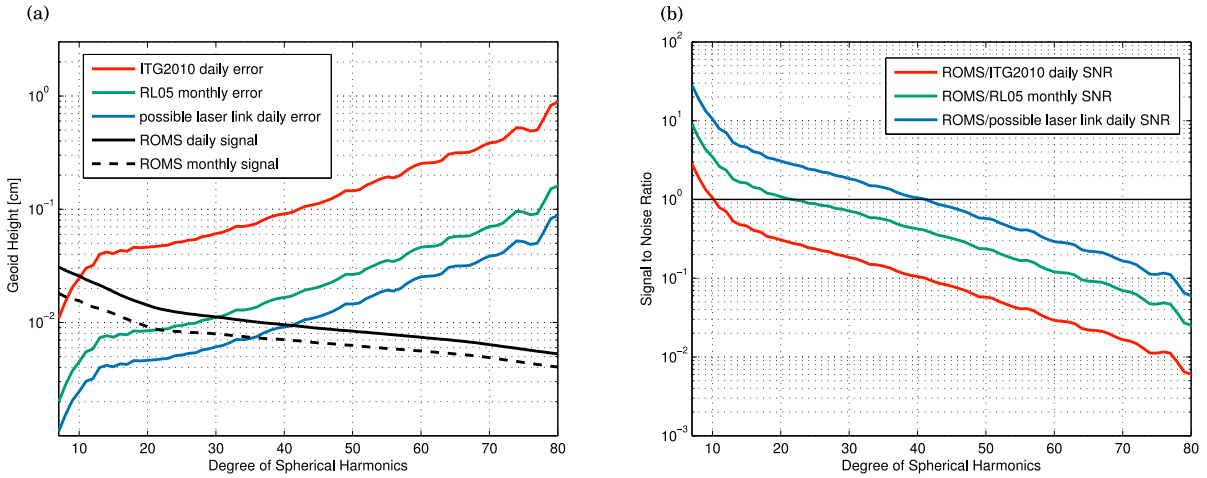

Figure 6.6: Estimates for (a) the degree-dependent noise level of GRACE measurements limited to the study domain as well as the amplitude of the signal derived from the ROMS model runs, and (b) the resulting signal-to-noise ratios, with the black line indicating an SNR≡1.

increasing degree except for the first couple of degrees which lose much of their weight in the process of localization. Therefore, only the low-degree parts of the signal are expected to be measurable by GRACE.

In Figure 6.6a, we show localized degree variances derived from our model output both for daily fields and monthly averages thereof. The temporal averaging reduces the signal by about a third. We base our comparison on a noise curve that belongs to monthly means of GRACE release 5 (RL05) data (Dahle et al., 2013, in print). In order to obtain a noise estimate for the daily ITG2010 data, we multiply it with a factor of $\sqrt{30}$ (T. Mayer-Gürr, personal communication, 2013), thereby accounting for the smaller amount of observational data incorporated into one daily field. The standard error of the mean decreases with the square root of the sample size, and for daily fields, only 1/30-th of the data is available compared to monthly fields. Multiplying this curve with a factor of 0.1 gives us the expected noise level for a possible follow-on GRACE mission. An tenfold error reduction is a rough estimate expected due to the implementation of more precise satellite ranging conducted with a laser instead of with microwaves as in the current system.

Considering the SNR curve for the current ITG-Kalman product in Figure 6.6b, we see that the simulated gravity signals are currently detectable, if at all, only when they exceed a spatial scale of 2000 km (corresponding to degree 10), which Agulhas rings certainly do not. The detectability of simulated oceanic signals gets better for the monthly GRACE data, allowing for signals down to a scale of 1000 km (degree 20). This comes closer to the actual diameter of Agulhas rings, which can be hard to determine precisely Schouten et al. (2000), but has been estimated to around 300 km (Lutjeharms, 1981; Schouten et al., 2003). Unfortunately, the monthly averaging of the GRACE data conflicts with the transient nature of the phenomenon. Nevertheless, improved reprocessing of the current GRACE measurements may bring the errors down just enough to measure at least large, strongly barotropic rings. The hope for GRACE measurements of Agulhas rings in the Cape Basin lie, however, in the GRACE follow-on mission

with laser linkage. With a sensible compromise between temporal and spatial resolution, OBP signals caused by Agulhas rings will be an ideal benchmark for this future satellite mission.

6.4 Summary

We created a setup of the ROMS ocean model to simulate regional ocean dynamics around South Africa, including the Agulhas Current and a segment of the ACC. Results from an 8-year simulation have been validated with satellite altimetry, showing that the model setup is able to capture the essential features of ocean circulation in the region. The mean SSH field is well represented in the model. The standard deviations of SSH show maxima in the correct locations, with limits in the Return Current and the exact path of the ACC which are not further analyzed in this study. Spectral analysis of SSH variations in three representative locations show that variability in the model setup is occurring on the right time scales.

Comparing fields of OBP variability from the model with gravimetric measurements from the ITG-Kalman solution and with in-situ PIES bottom pressure signals, we corroborated the OBP simulated by the model at the locations where in-situ measurements are available and identified a shortcoming of GRACE in measuring the strong OBP footprint of Agulhas rings in the Cape Basin.

We finally explored the potential of current and future satellite gravimetry products to detect the simulated spatial distribution of OBP variability and show that the estimated accuracy of the planned GRACE follow-on mission will be just sufficient to measure the OBP footprint of large, barotropic Agulhas rings.

6.5 Conclusions

This study adds to the existing work about ocean circulation throughout and around the Agulhas Current, one of the strongest currents in the world's oceans. It deals with ocean bottom pressure measured locally at a few locations throughout the region and globally with satellites. Combining these two independent measurements of the variable and extending the analysis with the aid of a regional ocean model, we provide an estimate of the location and amplitude of strong eddy-induced OBP signals throughout the region. The results can motivate future modeling efforts in the region focussing on geodetic observables since they hint at an area of prominent mass variations on small scales.

Simulations of ocean bottom pressure are also needed for the processing of satellite- and land-based gravity measurements that need to be corrected for ocean effects. While our model in the current non-assimilating setup cannot be used for de-aliasing purposes, we showed that de-aliasing products need to be obtained from high-resolution, most likely regional, model setups in order to capture the strongest non-tidal mass variations. Future solutions for the GRACE satellite data should be investigated for the presence of significant OBP signals off the South African coast, since new data processing algorithms might be able to measure signals here that, up to now, are most likely drowned in noise and smoothing. The signals identified take place

on temporal (weeks to months) and spatial (hundreds of kilometers) scales that make them a promising objective for a GRACE follow-on mission.

One immediate way to extend this study is to analyze longer measurement time series. An extension of the in-situ OBP measurement time series would provide better estimates of the local spectra and make the identification of Agulhas rings in the OBP signal more reliable. More data from additional measurement sites might also hint at other interesting regions of non-tidal OBP variability. For instance, the collection of data shown by Macrander et al. (2010) indicates that locations in or around the Kuroshio Current, the Malvinas Current, or the Drake Passage might be suitable as kinetic energy is high here as well (Thompson and Demirov, 2006).

This study showed how Agulhas rings can leave a footprint in fields of OBP variability throughout the Cape Basin. Of course, other physical effects play a role for this variable, too. For instance, coastal and topographic features are accompanied by characteristic resonances that can be excited by local wind fields, an effect that would be superimposed on the turbulence-induced OBP variability. While the length scales and frequencies of the dominant OBP anomalies in our simulations show that the signals are predominantly eddy-induced, a way to extend this study would be to separate and quantify these additional effects.

Studies of OBP phenomena of the spatial extent of mesoscale eddies would also benefit from improved GRACE solutions. Especially the planned GRACE follow-on mission, equipped with more precise laser satellite-satellite ranging instead of the current microwave-based system, might make it possible to bring all three data sets, GRACE, PIES, and ROMS, in agreement about OBP amplitudes off the South African coast.

Chapter 7

Detecting Crustal Deformations Resulting From Ocean Bottom Pressure Variations

The previous chapter described spatial and temporal OBP variability in a limited ocean area of particularly strong mesoscale circulation. OBP — or, more generally, mass distribution — is one of the central variables in the geodetic description of the Earth. The Earth's geometric shape is another one. In the oceans, this geometry manifests itself as SSH, while on land, it is detected as crustal deformation.

The two variables, mass distribution and crustal deformation, are connected on the Earth's surface which, depending on the time scale considered, reacts elastically or viscoelastically to shifting loads. Crustal deformation is caused by a wide range of processes: Tides within the solid Earth, the ocean, or also the atmosphere, are one major factor. Another factor consists of continental hydrological processes, especially in areas where large river systems act as reservoirs and produce a large, mostly seasonal, signal. This is the case, for instance, in the Amazon and the Congo Basins. Mass variation caused by glaciers and ice sheets are a further source of crustal deformation. The seasonal signal produced by regular partial melting of glaciers yields an elastic deformation, while the shifts from glacial to interglacial periods induce viscoelastic deformations (*glacial isostatic adjustment*, GIA).

The mathematical description of deformational processes was part of the subject of Chapter 2. Now focusing on deformation only, the terms of Equation (2.17) describing self-attraction are neglected. Furthermore, the following investigations are limited to the non-tidal ocean-induced portion of vertical continental movements. It is not possible to measure this portion in isolation, since it is always superposed by the sum of the other effects described above. In many inland locations, it is also not the strongest of all detected signals. However, signals such as tides, hydrological loading, or atmospheric loading can be removed from the measurements when they are known theoretically or estimated with models. The remainder of the vertical crustal motion is then taken as the non-tidal oceanic signal.

When, as is done in the following chapter, in-situ measurements of crustal deformation are used to determine global fields of the same variable, it is also necessary to remove mesoscale contributions to the in-situ measurements. For example, a point measurement at a coastal location in South Africa, close to the Agulhas Rings described in the preceding chapter, would be influenced by the mass signal that these rings were shown to carry. For the global field of non-tidal ocean loading, the signal of the Agulhas Rings, spanning a few hundred kilometers, is negligible. In-situ measurements of crustal deformation used to reproduce a global oceanic signal therefore need to be corrected for such local influences. To this end, regional ocean models

such as ROMS in setups including data assimilation, for instance from altimetry, are valuable tools.

Even though crustal deformation is a rather indirect measurement of ocean mass distribution, it overcomes some of the problems other OBP measurements have. In-situ measurements of OBP with PIES are affected by spurious drift. Additionally, the measured signal can be dominated by local processes, as presented in the previous chapter. Due to the crust's rigidity, the deformational signal on land is influenced by processes occurring in a wider radius. In addition, it is more homogeneous in space, since the effects of small-scale processes cancel out or vanish in the distance. The alternative to in-situ OBP measurements is the GRACE satellite pair. GRACE data will, however, suffer from an exptected gap between the demise of the current satellite pair and the start of a follow-on mission.

Measurements of the Earth's geometry have a wider observational basis than those of its mass. The sea surface is covered globally with satellite altimetry, while GPS stations, Satellite Laser Ranging, and superconducting gravimeters provide hundreds of continental measurement locations combined. One of these measurement locations is the superconducting gravimeter in Sutherland, South Africa, for which Kroner et al. (2009) have exemplarily shown the possibility of removing all known contributions to the gravity signal, which here acts as an indicator of crustal deformation, ending up with a residual that estimates the effect of non-tidal ocean mass variability only. In that study, the order of magnitude of the residual was on the edge of detectability. For locations directly on the coast, though, the signal-to-noise ratio is considerably better. Since the removal of unwanted portions of the signal is laborious, it is desirable to determine a rather small number of locations for which this effort has to be made in order to come up with a reliable estimate of the global deformation field. The following chapter describes a method with this objective. It thereby provides a link between variations of mass and geometry, both caused by ocean circulation, and a link between local in-situ and global satellite measurements of geodetic variables. It also shows how to employ these links to close the gap between the current and the future GRACE missions.

Chapter 8

Reconstructing Global Ocean-Induced Crustal Deformations From Land-Based In-Situ Stations

Submitted as: Kuhlmann, J., I. Rogozhina, R. Dill, I. Bergmann-Wolf, and M. Thomas, 2013: Reconstructing Global Ocean-Induced Crustal Deformations From Land-Based In-Situ Stations. *Journal of Geodynamics*, **xx (xx)**, xx, doi:10.1016/j.jog.xxxx, `http://www.journals.elsevier.com/journal-of-geodynamics/`.

Abstract. We present a method for reconstructing a global, time-variable field of deformations of the Earth's crust caused by non-tidal ocean loading (NTOL) from a small number of local deformation measurements. This is achieved by the decomposition of the NTOL field into empirical orthogonal functions (EOFs), which we obtain from GRACE satellite data. With this method, we achieve the reproduction of a highly correlated deformational signal across 95% of the land surface and the reduction of residual continental deformation from up to 1 mm to mostly below 0.5 mm on monthly GRACE data. The extrapolation of the deformational signal into the time for which no global EOF patterns can be recovered, for instance due to an expected gap in the satellite measurements, is exemplarily shown. Further, the possibilities and limitations of applying the method on submonthly GRACE products are investigated. We conclude that the described method can be a useful complement to existing data sets of ocean mass-induced crustal deformation, especially for periods where no satellite gravity data is available.

8.1 Introduction

Determination of the variability of oceanic mass distribution in space and time is a crucial for the understanding of a wide range of processes in the ocean, including sea-level rise, ocean tides, and wind-induced currents. The Gravity Recovery And Climate Experiment (GRACE, Tapley et al., 2004; Chambers et al., 2004; Schmidt et al., 2006) has been designed with the express goal in mind to better measure ocean mass variability. The mission has been a scientific success and provided insight into topics as diverse as Antarctic ice mass changes (Sasgen et al., 2007), the continental hydrological cycle (Wahr, 2004), and global ocean mass variations (Chambers et al., 2004). The two satellites are estimated to reach the end of their lifetime a few years before a follow-on mission, scheduled for 2017, will have been launched. Since no comparable satellite systems are available, the resulting gap in the data will need to be filled with in-situ data and best estimates for the global distributions of variables that GRACE observes. A reconstruction of the deformation fields based on Empirical Orthogonal Functions (EOFs) from GRACE data and corresponding Principal Components (PCs) from in-situ deformation measurements corrected for non-oceanic effects could potentially help to close this gap when fields of non-tidal ocean load-induced crustal deformations (NTOL) are needed.

GRACE data have been useful for numerous oceanographic studies (e.g. Cazenave et al., 2009; Macrander et al., 2010; Janjić et al., 2012), even though it remains challenging to come up with good ocean mass estimates based on the satellites' measurements. Extensive processing of the data is necessary in order to account for artifacts and unwanted effects on the data such as resolution-dependent noise in the provided spherical harmonic coefficients (e.g. Kusche et al., 2009), leakage of continental signals into oceanic areas (Guo et al., 2010), or solid Earth and oceanic tides (Tapley et al., 2004), only to name a few. The EOF-based method to reconstruct a global NTOL field from a small number of in-situ measurements described in this paper may thus be useful, beside the possibility of filling the expected GRACE gap, to create a data set that can serve as a "ground truth" for the GRACE data. Using EOFs from an ocean model, it would provide the same variables as GRACE does but from independent sources.

Such a reconstruction would be needed to be built upon a data basis which consists of in-situ time series of observed crustal deformation. There are several different measurement systems that can provide this type of information: GPS stations measuring the vertical position as travelling time of signals emitted by satellites whose tracks are precisely known; satellite laser ranging, working similarly, but based on a signal emitted from the ground and merely reflected by a satellite; and superconducting gravimeters (SGs) measuring the gravity field which varies due to a number of processes, among them the vertical movements of the local Earth crust. Since the total number of measuring locations is large, this data basis should leave the choice of optimal positions for in-situ time series of crustal deformation on the globe relatively open. While it is obvious that the ocean-induced signal is strongest at the coast, it is unclear where exactly at the coast good positions for stations serving our aim would be. For instance, should the measurements be located where the highest amplitudes of ocean-induced crustal deformation is expected, or should the focus rather be on a uniform distribution over the globe? Should they be placed on small islands, close to the generating mass fields, or on the continental edges, close

to the regions where the calculated corrections are actually needed? And how exactly would the space between the measurement locations be optimally filled? In this paper, we suggest a method that provides an answer to these questions.

Hughes et al. (2012) proposed as a measure of total ocean mass variability one single ocean bottom pressure (OBP) mooring in the central Pacific. The method described in this paper can be seen as an extension thereof. Yet, in our case, the measurements need to be performed on land, and we attempt to measure not only the globally integrated ocean mass, but a spatial distribution of its impacts. We will produce such an estimate with the help of EOFs, which Lorenz (1956) introduced into meteorology and which thereafter have been widely used for purposes of smoothing, prediction, data reduction, and extracting modes of variability (Hannachi et al., 2007). Smith et al. (1996) have established a method to reconstruct Sea Surface Temperatures from ship track data using EOFs, and Yang et al. (2010) have investigated EOFs as a method to optimize sensor placement in a small ocean area to measure velocity fields. We follow a similar approach, with the limitation that the measurements of crustal deformation that we rely on can only be taken outside of the ocean area and therefore consist of a quantity that is only indirectly linked to the generating field.

8.2 Data

We use measurements of the gravity potential induced by non-tidal ocean variability from the GRACE gravity satellite mission and employ them to compute the crustal deformation. The GRACE satellite pair measures inter-satellite distance to estimate the gravitational effect of mass redistribution within the Earth system. We use GRACE coefficients from the GFZ RL05 solutions (Dahle et al., 2013) and from the ITG-Kalman solutions provided by the Institut für Theoretische Geodäsie, University of Bonn (Kurtenbach et al., 2009). The GFZ RL05 data comes as monthly solutions, smoothed with the non-isotropic, degree-dependent DDK1 filter (Kusche et al., 2009). The ITG-Kalman data is based on a Kalman Smoother approach in order to come up with daily fields of mass variations. In both solutions, the GAB product, i.e. data describing non-tidal ocean variations only (Flechtner and Dobslaw, 2013) has been added back to receive the ocean-induced gravity potential. Model-based estimates for continental and atmospheric contributions have been subtracted from the initial data, so we retain a purely oceanographic signal. In both solutions, continental leakage has been reduced with a Gaussian filter of 300 km halfwidth radius. In this study, measurements from 2003 through 2012 are used.

From the GFZ RL05 GRACE data, we obtain global monthly fields of gravity potential which we subsequently transform into crustal deformation. To this end, we multiply the coefficients C_{nm} and S_{nm} with the degree-dependent factor $h_n/(2n+1)$, where h_n is the n-th load Love number (Farrell, 1972). The elastic properties of the Earth crust is described by a set of load Love numbers, based on the PREM Earth model (Dziewonski and Anderson, 1981) from `http://gemini.gsfc.nasa.gov/agra/`. We employ the ITG-Kalman data for NTOL variations on shorter time scales, either averaged over 10-day periods or on the original daily grids.

8.3 Method

We attempt to reconstruct a 3D NTOL field (one temporal and two spatial dimensions) from a small number of deformation point measurements (temporal dimension only) with the help of EOFs. By computing the NTOL field from the GRACE gravity coefficients, we obtain a 3D field (two spatial dimensions and one temporal dimension) of ocean-induced crustal deformations. Decomposition of this field into area-weighted EOFs generates n_t EOF patterns in space and n_t associated principal component (PC) time series, where n_t is the number of time steps in the data set. The EOF patterns are sorted by decreasing explained variance. We then apply a land mask in order to reduce the EOF patterns to the contintental area where actual measurements are possible. In order to find the optimal measurement location for each EOF, we compute the 2D field describing the relative variance of the i-th EOF with respect to the sum of all other EOFs. The coordinates where this relative variance reaches its maximum value describe the optimal location to measure the evolution of EOF_i in time (marked as circles in the following figures). Since the PCs cannot be measured directly, the deformation time series at this location replaces the i-th PC in the reconstruction of the deformation signal. The EOF patterns themselves cannot be measured either; they need to be determined a priori from GRACE data. The number of EOF patterns considered is variable, limited by the decreasing maximum relative variance, which corresponds to a signal-to-noise-ratio. The synthesis of EOF patterns with deformation time series yields a 3D field of crustal deformation which can be extended toward periods where no comprehensive satellite measurements are available, or it can serve as a ground truth to compare satellite measurements against. In the latter case, the EOF decomposition needs to be obtained from a data set unrelated to the satellite data, e.g. from a numerical model. We will focus on the first case, where the EOF patterns are obtained from GRACE data. The reconstruction can be performed with complete EOF patterns containing values both for land and ocean grid points.

The described method is based on a few assumptions. First, it is necessary that EOF patterns remain constant over time and only the loading described with the PCs varies, even beyond the time frame that was used to estimate the EOF patterns. This assumption is essentially the idea that EOF analysis in Earth science is based on, since an EOF analysis in this context translates to a linear decomposition into basis functions of space and expansion functions of time (Hannachi et al., 2007). EOF analysis has already been applied to global fields of ocean mass variation (Bingham and Hughes, 2006; Chambers and Willis, 2010), so this assumption is reasonable. We will nevertheless investigate its validity for our application later on. Second, we need to assume that a reconstruction of the initial signal with the first few EOFs only is a meaningful approximation of the total signal. The quickly decreasing contribution of additional EOFs to the signal is a factor determining the goodness of our reconstructed deformation signal. Third, it is necessary that, for each EOF of OBP-induced deformation, there exists a location on land where it is responsible for a large enough fraction of the local deformation signal that a replacement of the respective PC with it yields useful results. The consideration of more EOF patterns with a disadvantageous signal-to-noise ratio will also be investigated in the following. Beyond that, local deformation time series are useful for reconstructing global fields only if they

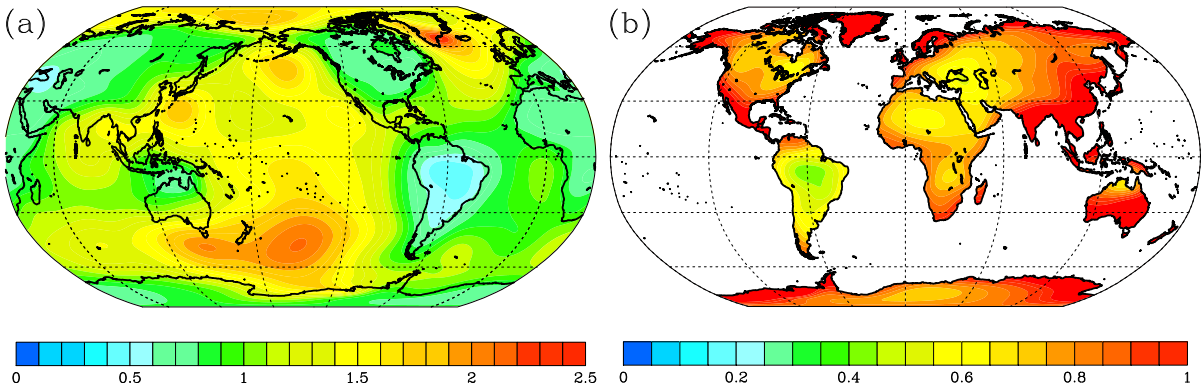

Figure 8.1: Standard deviation of ocean-induced crustal deformation in millimeters computed from monthly GRACE NTOL data for the period from 2003 through 2010, (a) globally and (b) showing only the values on land.

are representative for a larger region as opposed to being mainly influended by near-field effects. And fourth, the method is based on the separability of deformations caused by ocean dynamics from the residual caused by hydrological processes, atmospheric pressure variations, tides, and so forth. van Dam et al. (2012) have used measurements of the vertical movements of GPS stations with the goal of extracting NTOL-related signals, and Williams and Penna (2011) have determined that contributions from NTOL can reach or even exceed those from atmospheric loading in GPS data. Kroner et al. (2009) have shown that the non-tidal ocean-induced signal is detectable when all other known sources of crustal deformation are accounted for at a few locations on the globe where SGs are positioned. This processing requires a good knowledge of local conditions and will not be done in this paper, but considering the available literature, we assume that it is essentially feasible. Especially for atmospheric pressure, good data sets are widely available; hydrological processes can be a major influence in areas such as the Amazon delta, but their impact is often minor on coastal locations far from river mouths; and tides are principally well known because of their clearly defined frequencies. For a detailed description of the corrections which need to be made to in-situ SG data when a comparison to GRACE is attempted, see Crossley et al. (2012).

8.4 Results

Figure 8.1 shows the standard deviation of daily ocean-induced crustal deformation in the GFZ RL05 GRACE data. The values show a maxima of 2 to 2.5 mm in the Antarctic Circumpolar Current (ACC) and in the North Pacific. The maximum on the coast of Greenland is presumably caused by continental leakage. The elevated variability in the Pacific is evidence of the Earth's crust acting as a low-pass filter in the spectral domain, producing a relative amplification of the large-scale signals that occur in the largest ocean basin, the Pacific. The varying ocean masses yield the largest deformations of up to 2 mm on monthly scales within the ocean basins, with crustal deformation on land remaining around 1 mm and decreasing away from the coasts. Nevertheless, the coastal areas with deformations of 1 mm span much of North America, northern

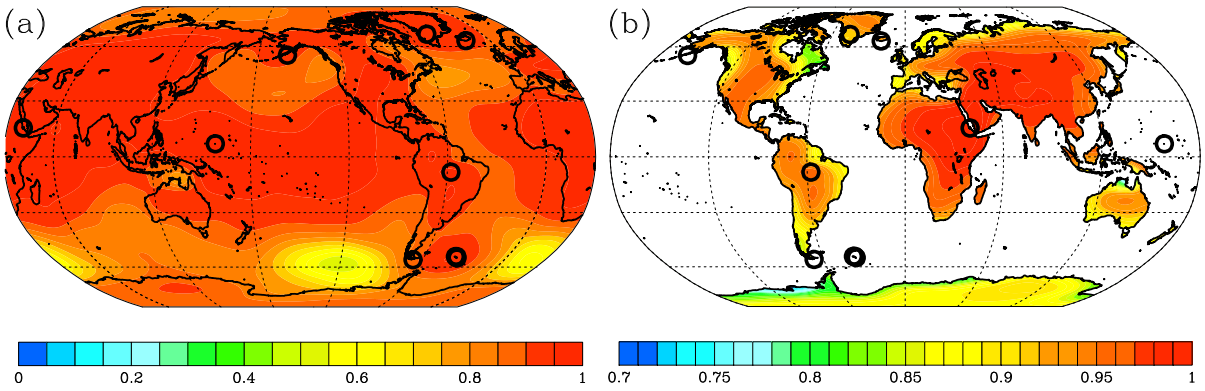

Figure 8.2: Correlation coefficient between the deformation time series at each grid point and the corresponding reconstructed deformation time series computed from monthly GRACE NTOL data with 10 EOFs and the in-situ deformation at the identified optimal locations for the period from 2003 through 2010, (a) globally and (b) showing only the values on land.

and western Europe, East Asia, Australia, and Antarctica (Figure 8.1b). The length of the coastline with high standard deviations, thus in principle suited for the placement of in-situ deformation measurement devices, makes a choice only from these results difficult. Considering that the strongest NTOL effect is centered in the ocean basins themselves, a first guess might also be that placement of measurement devices on small islands, many of which are not visible in Figure 8.1, is optimal. The values obtained are similar to the ones obtained from the ECCO ocean model by van Dam et al. (2012), who found root-mean-square variability of radial surface displacement to fall between 0.2 to 2.5 mm for most of the locations considered.

In order to make a choice of optimal in-situ measurement locations more objective, we employ the method described in Section 8.3. We reconstruct a time series of ocean-induced crustal deformation from the GFZ GRACE RL05 data during the years 2003 through 2010 from EOF patterns obtained from the same time period's data and the local deformation time series at ten grid points chosen with the algorithm described in Section 8.3. We correlate the initial deformation time series with the reconstructed time series at each grid point and show Pearson's correlation coefficient in Figure 8.2. Figure 8.2a shows the correlation throughout the globe. The optimal in-situ locations are widely distributed across the continents and across island locations. The locations are all close to the coast except for one position in South America. Some of them are on islands, which in terms of data quality is ideal for a study of this kind, since the small land area generates only a small hydrological signal which needs to be corrected for. Nevertheless, many of the determined stations are placed on the mainland. In a few cases, multiple stations are placed at identical or very proximate locations, which reduces the efforts of possible data acquisition even further. The quality of the reconstruction in terms of correlation coefficient reaches the highest values in the Tropical oceans and on the continents: in Asia, most of Europe, throughout Africa, in North and South America, and in Australia, the correlation coefficient is above 0.9. Across the remainder of the land surface, especially in Antarctica, it varies between 0.7 and 0.9. Crustal deformation in the ice-covered regions of Greenland and

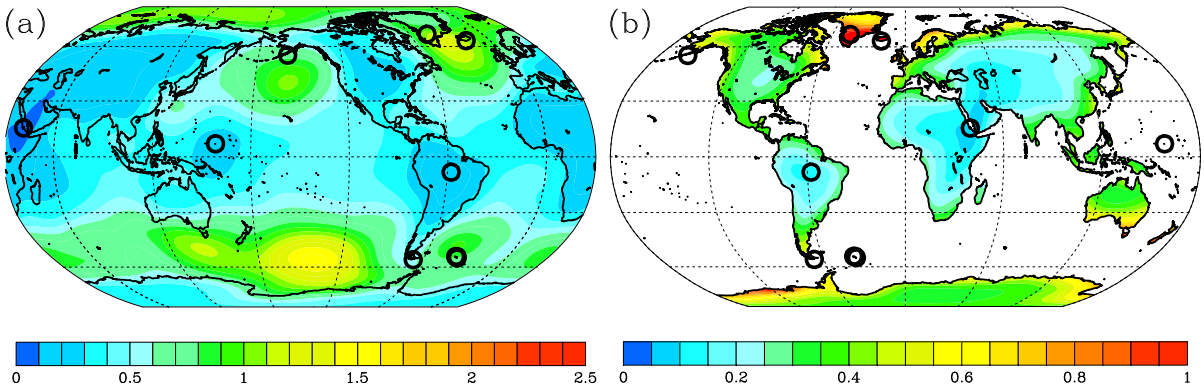

Figure 8.3: Root-mean-square difference in millimeters between the deformation time series at each grid point and the corresponding reconstructed deformation time series with 10 EOFs and the in-situ deformation at the identified optimal locations for the period from 2003 through 2010, (a) globally and (b) showing only the values on land.

Antarctica is strongly influenced by post-glacial uplift and the annual cycle of ice mass load, so inferring an NTOL signal from GPS time series in these regions is, in any case, ambitious. Additionally, the latitude-dependent weighting of the gridded NTOL signal proportional to the surface area makes the polar regions less essential. In East Africa, remarkably, one station suffices to recover correlations of above 0.9 throughout Eurasia and Africa. This is probably related to the deformation signal in the Indian Ocean being mostly a seasonal signal which is relatively easy to capture with an EOF approach.

When comparing the reconstructed deformation field with in-situ data, a crucial variable besides correlation is the difference between the true field and the approximation. If this difference is below the accuracy of in-situ deformation measurements, the proposed correction is useful. We show the global field of root-mean-square differences for the monthly GFZ GRACE RL05 data in Figure 8.3a and the same data restricted to the land surface in Figure 8.3b. The first notable effect is the discrepancy between continental values of 0.1 mm to 0.5 mm and oceanic values which are around three times larger. The high spatial autocorrelation of continental deformation makes it a good target for the EOF-based method. In the areas of maximum OBP variability in the ACC and the North Pacific, the recontruction can reduce the residual by around 0.5 to 1.0 mm or 25 to 50%, while in the Tropical oceans, the residual is reduced by about two thirds. If one is to focus on land areas (Figure 8.3b), there are considerable improvements on all continents. On most land surfaces except Greenland and Antarctica, the residuals stay at 0.5 mm or below which means a 50% to 70% reduction compared to the computed total NTOL signal.

Considering that the extraction of the non-tidal ocean-induced part of the in-situ deformation signal at a GPS, SLR, or SG station is relatively laborious, especially when a strong hydrological signal is present in the vicinity, it is desirable to obtain a good reconstruction of the global deformation field with as few in-situ stations as possible. In Figure 8.4, we therefore show the fraction of the globe throughout which the correlation between the deformation field and its reconstruction (as shown in Figure 8.2) exceeds a threshold value of 0.85. In the case of monthly

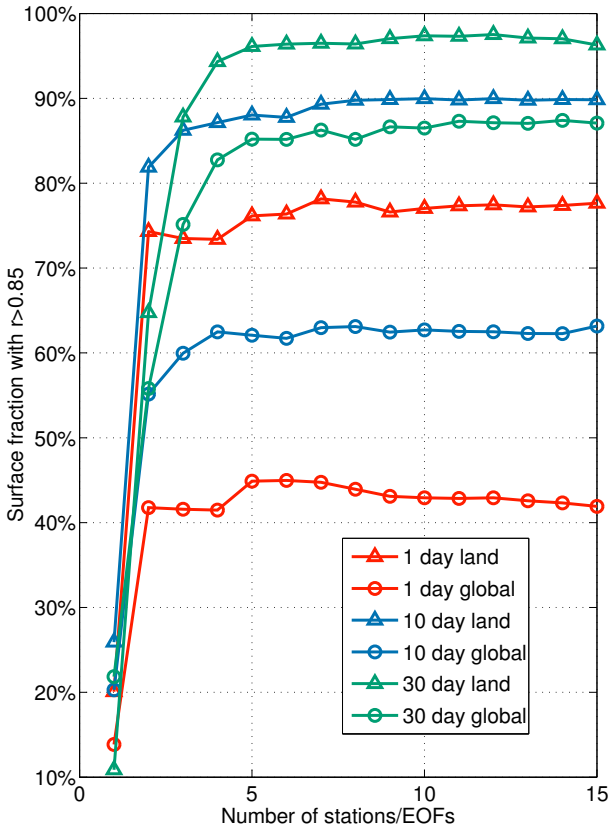

Figure 8.4: Fraction of land area and global surface area in the reconstruction where the correlation exceeds a threshold of 0.85 based on monthly GFZ GRACE data, 10-day averages of ITG GRACE data, and daily values from ITG GRACE.

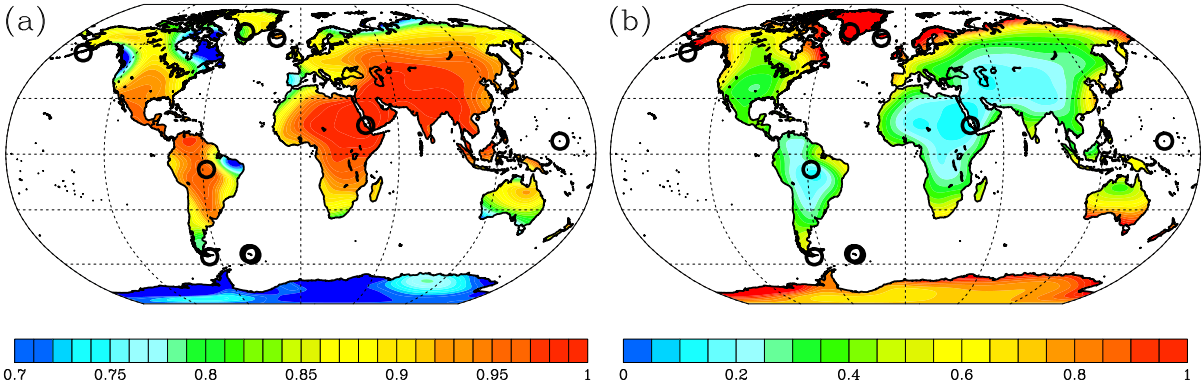

Figure 8.5: Correlation coefficient (a) and root-mean-square difference in millimeters (b) between the deformation time series at each grid point and the corresponding reconstructed deformation time series with 10 EOFs and the in-situ deformation at the identified optimal locations. In this case, the EOFs have been obtained from the years 2003 through 2010 of monthly GFZ GRACE data and the comparison is performed for the years 2011 through 2012, from which only the time series of single grid boxes have been taken.

fields on the entire globe (green circles), this fraction reaches 85% with 5 EOFs and does not increase considerably when more patterns are added. If one takes into consideration only the land surface, a useful reconstruction can be performed for more than 97% of the area with 10 EOF patterns or more.

When the reconstruction of faster signals is required, which we consider by using the daily ITG-Kalman GRACE data or 10-day averages thereof, the portion of the globe with well reconstructed time series reduces to around 43% and 63%, respectively. Considering land surface only, the maximum fraction of well-reproduced surface area reaches 77% and 89%.

In light of these figures, we conclude that the consideration of 10 EOFs is sufficient for our purpose of computing NTOL fields mainly on the continents. For most data sets, even 5 EOFs would suffice, so in real-world applications, where the addition of more time series is costly, this might also be a reasonable choice. While the consideration of more patterns does not further improve the reconstruction, which can be seen by the flatness of the curves in Figure 8.4 beyond a number of 10 at most, it is also mostly not detrimental since the small explained variance of the higher-order EOFs makes their contribution rather small.

Up to now, the shown reconstructions have essentially reproduced the input signal, although from a drastically reduced data basis. A more realistic use case is the extrapolation of deformation time series into the future or maybe even in the past, where GPS, SG, and SLR data were available, but GRACE data was not. In Figure 8.5, results from such an extrapolation are shown. The deformation EOFs have been obtained from GFZ GRACE RL05 data of the years 2003 through 2010. The reconstruction, however, has been performed with GRACE-derived local deformation time series of the following years of 2011 and 2012. Figure 8.5a shows the correlation coefficient between the deformation field based on the GRACE measurements and its reconstruction for the monthly data. Throughout much of the continental surfaces, the correlations exceed 0.8, only in Antarctica and on the eastern and western coasts of Canada,

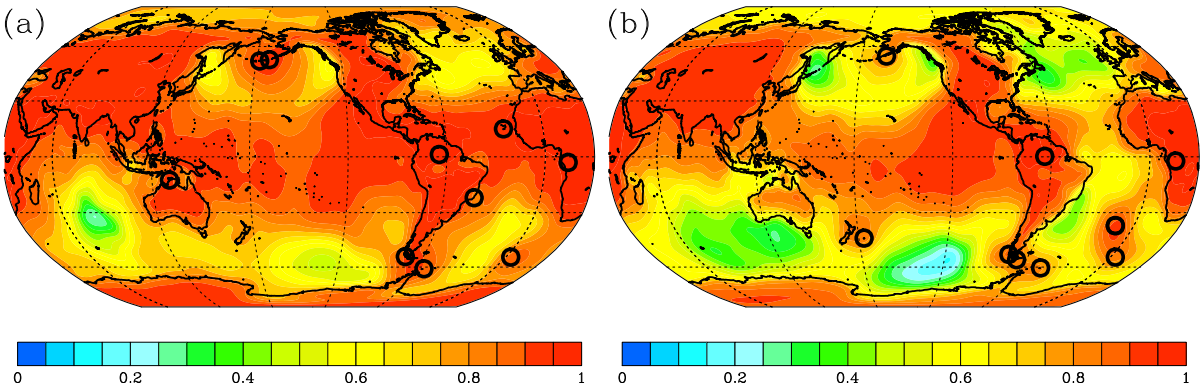

Figure 8.6: Correlation coefficient between the deformation time series at each grid point and the corresponding reconstructed deformation time series computed from ITG GRACE NTOL data with 10 EOFs and the in-situ deformation at the identified optimal locations for the year 2007, based on (a) 10-day averagees and (b) daily data.

correlations remain at 0.7 or below. Considering the root-mean-square differences (Figure 8.5b), the accuracy of the reconstruction is below 0.5 mm on most land surfaces except in Arctic and Antarctic regions. The results are slightly weaker than those obtained for the reconstruction of monthly averages on identical time periods (Figure 8.3), but still provide a useful improvement compared to Figure 8.1.

Temporal and spatial scales of non-tidal oceanic mass variations are often linked, with fast signals generally being of smaller extent. As a result, the performance of the method on daily fields or 10-day averages is supposed to be weaker than on monthly fields. Figure 8.6a shows the correlation coefficient of the deformation field with its reconstruction considering 10-day averages of ITG GRACE fields. Correlations are similar to what had been obtained from GFZ GRACE data (Figure 8.2a), with correlations of 0.8 and above on the continental surfaces and certain weaknesses in the ACC, the North Pacific, and the North Atlantic, where correlations regionally drop to 0.6, and the Indian Ocean, where a minimum of 0.4 is reached. The small spatial scales of mass variations in the extratropics and the long distances to coasts in the case of the ACC make the signals harder to determine. It is also notable that the station distribution in Figure 8.6a shows a cluster around the South Atlantic, which might make some of the information from the time series redundant.

Testing the method for even faster variations with the daily ITG-Kalman data (Figure 8.6b), the correlations throughout large parts of the ocean drop to 0.6 and below. On the continents, the reconstruction remains a lot more meaningful with correlations of 0.7 and above. The rigidity of the crust leads to the deformations on continental surfaces being autocorrelated in space much more than it is the case for ocean surfaces. When the reconstruction of an NTOL signal usable at GPS stations is the primary goal, the method still performs well on the daily fields. It is noteworthy, however, that the optimal locations for sensor placement in Figures 8.6a and 8.6b differ from those shown in the earlier figures for the GFZ GRACE RL05 data. The choice of actual deformation time series from in-situ stations therefore needs to be preceded by the calculations of EOF patterns from the global NTOL data set that is to be used later on.

8.5 Summary

We have adapted a method for reconstructing a high-dimensional field from low-dimensional measurements with the aid of EOFs to the case of crustal deformations induced by non-tidal ocean loading (NTOL). The GRACE satellite data shows crustal deformations of up to 2 mm in the ocean and above 1 mm in many continental areas, especially in proximity to the coast. We deconstruct the deformational fields into EOFs and determine optimal locations for measurements to replace the corresponding PCs with local time series of deformation from the relative variance of the EOF patterns. It emerges that a combination of island and continental coastal locations spread out over the globe is optimal in the case of the investigated data sets. Particularly for deformational time series on monthly temporal scales, the reconstructed data achieves correlations with the initial data of mostly above 0.85 on the continents and in the oceans. The root-mean-square error of the deformation for continental locations can be reduced to 0.5 mm and less, which is sufficient in view of the accuracy of currently used in-situ measurements.

For a useful reconstruction of NTOL fields, a set of five to ten time series of in-situ measurements is estimated to be sufficient. With a data basis of this kind, an extrapolation of a satellite-derived data set into a time period where no gravitational satellite data is available is feasible, especially when the goal is to reconstruct continental deformations or when signals of monthly or longer periods are considered.

Using NTOL patterns from daily ocean mass variations, the accuracy of the reconstruction decreases especially in strongly dynamic regions of the oceans where spatial autocorrelations of the dominating processes are small.

8.6 Conclusions And Outlook

There are several applications for the method that we propose for reconstructing global deformation fields from in-situ data. Besides the possibility to complement satellite gravity measurements from GRACE with an independent data set, the extension of fields of mass variability into the time period where GRACE data will become unavailable may be a particularly beneficial one. Considering the deficits of the reconstruction on daily time scales in the Southern Ocean, where ocean mass variability is especially strong, however, the applications need to be chosen carefully and may not be a global replacement of the GRACE data. Here, the use of in-situ bottom pressure recorders to measure the oceanic mass signal directly seems more promising. The risk of this approach, however, is a possible contamination of bottom pressure data with local processes such as ocean eddies, which would make an approach similar to the one described in this work questionable.

When it comes to ocean-induced deformation on the continents, the obtained reconstructions are generally more accurate than in the ocean, so the separation of ocean-induced signals from the measurements of inland GPS stations can be a further application. In this case, the benefit in comparison to other methods is that no a priori knowledge about the nature of the local deformations is necessary. Alternatives, such as a sine-shaped fit to provide an

analytical seasonal cycle, or the spatial interpolation between a few stations to obtain a complete data set for the continental surfaces, make strong assumptions about the temporal or spatial behavior of the data that an EOF-based method does not need. Furthermore, in cases where the number of measurement locations is very small, EOF approaches are often more accurate than interpolations (Taylor et al., 2013).

Calculating the optimal locations of in-situ measurements for a few exemplary data sets, we have shown that these positions depend on the temporal resolution and the choice of input data for the computation of the EOF patterns. A consideration of five to ten in-situ locations is sufficient for the optimally reconstructed signal obtainable with the described method.

There are a few possible extensions which could serve to further refine the described method. Modifications of the EOF analysis, for instance with extended empirical orthogonal functions (EEOFs) or rotated empirical orthogonal functions (REOFs) (Hannachi et al., 2007) could be employed to possibly obtain a better differentiation of signals into different EOFs. Furthermore, it turned out that in some cases, almost identical locations were optimal for the determination of the same time series. In these cases, prescribing a minimum distance or combining two EOF patterns may be advantageous. Another possible modification is the choice of optimal locations based on the correlation of the respective PC with the local time series instead of calculating the maximum relative variance of EOF patterns.

The described approach does not need to be applied to global fields of crustal deformation but could also be employed in regional studies. Especially when hydrological or glacial instead of oceanic loads are considered, and mass distributions for a limited time period are available, it might be instructive, for instance, to reconstruct hydrological loading in the Amazon basin from a small number of South American GPS stations, or to reconstruct ice mass variability throughout Antarctica from a few time series of coastal GPS measurements.

Chapter 9

General Summary

This thesis dealt with the measurement and numerical simulation of sea level variations, particularly the temporal and spatial changes of its eustatic part described in terms of ocean bottom pressure (OBP). A variety of different topics emerged from this common theme: After providing the theoretical foundations for the calculation of the effects of gravitational Self-Attraction and Loading (SAL) induced by OBP variations, Chapter 2 reviewed the existing literature on this subject. Especially when and how to consider SAL and when to neglect it is a topic of ongoing dispute. From the assembled results, it becomes clear that implementing SAL into models of tidal variations is crucial to obtain correct amplitudes, frequencies, and phases of sea level variation. Meanwhile, for non-tidal processes, adding SAL fields as corrections in the post-processing is sufficient. Among the non-tidal contributions, the gravitational and deformational impact of continental water masses dominates. Scalar parameterizations of SAL do not provide satisfying accuracy, neither in tidal nor in non-tidal applications, thus a full consideration of SAL is to be preferred. SAL modifies both tidal and non-tidal amplitudes by around 10%.

The results from Chapter 4 support these conclusions. The full implementation of SAL into the global baroclinic OMCT model shows that modifications of sea level reach between 0.6 and 0.8 cm. Due to the remote action of SAL, the effects are important especially for the relative impact in calm regions of the ocean. Effects of SAL on water velocities as well as on heat and salt distributions — which the baroclinic model, in contrast to earlier, purely barotropic setups, captures properly — are shown to be of minor importance. The increases in computing time for the decomposition of the field of OBP anomalies into spherical harmonics, the application of Love numbers, and the synthesis into a correcting field to the pressure gradients needed for the computation of horizontal velocities, remained at around 16%. Increasing computational efficiency with the application of scalar approximations turned out to be inadequate since the appropriate scalar factor is too variable in space and in time.

One way towards a better representation of OBP-related processes unresolved in the heretofore investigated global ocean models is the increased spatial resolution that regional ocean models provide. Chapter 6 provided such a regional application, focussing on the simulation of mesoscale variability in the Agulhas region around South Africa and its impacts on OBP variability. In the specifically built setup of the regional ROMS model, boundary values from the global OMCT model used in Chapter 4 provide a representation of the surrounding ocean. Meanwhile, the processes of eddy generation, transport, and intensification in the Agulhas basin are modeled entirely with the higher-resolution ROMS model. The simulated eddies are absent from the OMCT model output, but the ROMS simulations as well as satellite altimetry data show that they are the dominant contributor to sea level variations on weekly to monthly time scales in the region.

In the following, the results from the ROMS model provided a link to smaller spatial scales. To this end, in-situ data from PIES, devices placed on the sea floor to measure OBP variability, was compared to the simulations. The measurement data corroborated the model results in terms of location and spectral signature of strong, Agulhas ring-induced OBP signals off the South African coast. Chapter 6 also provided a link to global satellite observations of OBP with the GRACE satellites. The modeled Agulhas rings are vast enough, slow enough, and have a large enough amplitude that a modest increase in temporal and spatial resolution of the GRACE remote sensing system would make them detectable from space. GRACE data has contributed to the quantification of global eustatic sea level rise, but mesoscale phenomena in the ocean have, up to now, not shown up in the data. The analysis of regional ocean model simulations in Chapter 6 shows that this will change once the planned GRACE follow-on mission is in orbit after the year 2017.

The expected gap in GRACE measurements also motivated the study in Chapter 8. The accuracy and global coverage of GRACE data is difficult to achieve with complementary systems. An attempt in this direction is to make use of the leading patterns of variability that have emerged from the last decade of GRACE data and complement them with in-situ measurements of crustal deformation which are available at many locations on the continents. Focussing on non-tidal ocean loading, described as one component of the SAL effects described in Chapters 2 and 4, these variability patterns result from OBP variations only. Chapter 8 showed that if in-situ measurements from GPS stations, satellite laser ranging stations, and superconducting gravimeters are corrected for impacts from non-oceanic contributions, global distributions of non-tidal ocean loading can be recovered for periods where GRACE data is not available.

The reconstructed monthly deformation fields proved to be most accurate on the continents, where correlations above 0.85 are reached across 95% of the surface area and where the residual signal is reduced from up to 1 mm to mostly below 0.5 mm. On the continents, such a reconstruction is also of most use: if a few carefully processed stations suffice to reproduce a global signal, this signal can in turn be used to correct all other GPS time series for the effects of non-tidal ocean loading. Reconstructions of submonthly variations are less accurate due to the smaller spatial autocorrelations, particularly in the dynamically active and turbulent regions of the global ocean.

Chapter 10

Open Questions

In each of the topics of investigation explored above, there remain unanswered questions. Furthermore, the combination of the different topics offers routes for further research.

One possible enhancement of the SAL implementation into OMCT of Chapter 4 is the extension of the forcing field $\sum_{n=0}^{\infty} p'_{B,n}$, which in the present implementation considers OBP only, with other sources of mass variations. For instance, mass variations from the atmosphere, which are already present in the model as surface air pressure, or from hydrological processes, obtainable from additional input data, can be added. Experiments with an updated version of OMCT running at an increased resolution of $1^\circ \times 1^\circ$ (not shown) provide hints that rather small changes to local coastlines and bathymetry can drastically move sea level variability towards a more realistic state locally, but purely oceanic SAL effects have only small impacts in these regions. Considering other sources of mass variation potentially contributes to more accurate simulations of local resonances.

Global ocean models for interannual studies and long-term projections, however, retain other deficits where improvemets are more promising. For instance, the momentum transport from the atmosphere to the upper layers of the ocean relies on parameterizations which account for processes that cannot be precisely simulated in a coarse-resolution ocean model. An example of these parameterized processes is the surface roughness which depends on the wave height, partial ice cover, and the wind profile in the lower 10 meters of the atmosphere. For increased accuracy of modeled ocean currents, these issues are critical.

In the modeling of regional ocean dynamics around South Africa in Chapter 6, it emerged that temporal coincidence of specific Agulhas eddies in the model and the measurements is unachievable considering the chaotic process of eddy formation upstream in the vicinity of Madagascar. Overcoming this limitation by assimilating measurements of eddy locations, for instance from altimetry data, into ROMS, is a promising improvement of the current model setup which is currently being working on. It will permit to investigate the vertical structure of mesoscale eddies in the region in more detail and will also be helpful for the de-aliasing of satellite or land-based in-situ gravity data.

Using the EOF method described in Chapter 8, one could go back to the model output from Chapter 6 and determine optimal positions for measurements of ocean-induced crustal deformation in Southern Africa. A more direct approach, skipping the step of transforming mass variation into crustal deformation, is also possible: The method can provide information about where to place bottom pressure sensors within the Agulhas region that describe the behavior of leading variability patterns. The contamination of in-situ signals with mesoscale eddies may even turn out advantageous, since the regular translational speed of the eddies can provide useful patterns of spatial autocorrelation.

Similar approaches can also be carried out with methods of pattern recognition other than EOF analysis. For instance, the aggregation of similar time steps in the data with clustering

algorithms has been explored in Kothur et al. (2013). The results of the study concerned with the Agulhas region are still preliminary, and much depends on the precise definition of similarity between time steps or, in an extension of that work, similarity between time series at one grid point. Nevertheless, it may be possible to find locations where the signal of an in-situ sensor correlates well with the current state of the larger system. In that case, it would be possible to replace the measured fields of full spatial coverage with dominant patterns and information from in-situ time series, similar to what has been done in Chapter 8.

In principle, an implementation of the SAL effects investigated in Chapter 4 into the ROMS setup used in Chapter 6 is also possible, even though certain technical challenges would need to be overcome. These challenges arise from the parallelization of the ROMS model, which splits the region to be modeled into a number of sub-regions for which the evolution in time is calculated on seperate cores of the supercomputer. Only at certain points in the model code, information is exchanged between the sub-regions. The remote action of SAL would make additional information exchange of this kind necessary, potentially slowing down the model beyond the 16% increase of computing time that had been determined for the unparallelized OMCT model in Chapter 4. Otherwise, the consideration of SAL effects in the regional model, possibly with the addition of hydrological and atmospheric effects discussed above, might provide improved sea level patterns and modes of sea level variability in the region yet undetected.

The investigation of spatial and temporal variability of sea level and ocean mass remains a field of research where many intertwined processes need to be investigated separately in order to replace the global scalar value describing the projected mean sea level with a good estimate of spatial patterns. This work may have shed light on the workings of some of these processes, helping to understand, measure, and simulate them more accurately.

Bibliography

Abramowitz, M. and I. A. Stegun, 1972: *Handbook of Mathematical Functions*. United States Department of Commerce, 470 pp.
URL http://people.math.sfu.ca/~cbm/aands/

Accad, Y. and C. L. Pekeris, 1978: Solution of the Tidal Equations for the M_2 and S_2 Tides in the World Oceans from a Knowledge of the Tidal Potential Alone. *Philosophical Transactions of the Royal Society A: Mathematical, Physical and Engineering Sciences*, **290**, 235–266, doi:10.1098/rsta.1978.0083.
URL http://rsta.royalsocietypublishing.org/content/290/1368/235

Adams, J. C. and P. N. Swarztrauber, 2009: SPHEREPACK 3.2: A model development facility.
URL http://www.cisl.ucar.edu/css/software/spherepack/

Alexander, L., S. Allen, N. L. Bindoff, F.-M. Bréon, J. Church, U. Cubasch, and E. Al., 2013: Working Group I Contribution to the IPCC Fifth Assessment Report: Summary for policymakers. *Climate Change 2013: The Physical Science Basis*, number September 2013.
URL http://www.climatechange2013.org/images/uploads/WGIAR5-SPM_Approved27Sep2013.pdf

Backeberg, B. C., L. Bertino, and J. A. Johannessen, 2009: Evaluating two numerical advection schemes in HYCOM for eddy-resolving modelling of the Agulhas Current. *Ocean Science*, **5**, 173–190, doi:10.5194/os-5-173-2009.
URL http://www.ocean-sci.net/5/173/2009/

Baker-Yeboah, S., D. A. Byrne, and D. R. Watts, 2010: Observations of mesoscale eddies in the South Atlantic Cape Basin: Baroclinic and deep barotropic eddy variability. *Journal of Geophysical Research*, **115**, C12069, doi:10.1029/2010JC006236.
URL http://www.agu.org/pubs/crossref/2010/2010JC006236.shtml

Baker-Yeboah, S., D. R. Watts, and D. a. Byrne, 2009: Measurements of Sea Surface Height Variability in the Eastern South Atlantic from Pressure Sensor–Equipped Inverted Echo Sounders: Baroclinic and Barotropic Components. *Journal of Atmospheric and Oceanic Technology*, **26**, 2593–2609, doi:10.1175/2009JTECHO659.1.
URL http://journals.ametsoc.org/doi/abs/10.1175/2009JTECHO659.1

Beal, L. M., W. P. M. De Ruijter, A. Biastoch, and R. Zahn, 2011: On the role of the Agulhas system in ocean circulation and climate. *Nature*, **472**, 429–36, doi:10.1038/nature09983.
URL http://www.nature.com/nature/journal/v472/n7344/abs/nature09983.html

Biastoch, A. and C. W. Böning, 2013: Anthropogenic impact on Agulhas leakage. *Geophysical Research Letters*, **40**, 1138–1143, doi:10.1002/grl.50243.
URL http://onlinelibrary.wiley.com/doi/10.1002/grl.50243/fullhttp://doi.wiley.com/10.1002/grl.50243

Bindoff, N. L., J. Willebrand, V. Artale, A. Cazenave, J. M. Gregory, S. Gulev, K. Hanawa, C. Le Quere, S. Levitus, Y. Nojiri, and Others, 2007: Observations: Oceanic Climate Change and Sea Level. *Climate Change 2007: The Physical Science Basis. Contribution of Working Group I to the Fourth Assessment Report of the Intergovernmental Panel on Climate Change*, S. Solomon, D. Qin, M. Manning, Z. Chen, M. Marquis, K. Averyt, M. Tignor, and H. Miller, eds., Cambridge University Press, Cambridge, United Kingdom and New York, NY, USA, chapter 5.
URL `http://centaur.reading.ac.uk/770/`

Bingham, R. J. and C. W. Hughes, 2006: Observing seasonal bottom pressure variability in the North Pacific with GRACE. *Geophysical Research Letters*, **33**, L08607, doi:10.1029/2005GL025489.
URL `http://doi.wiley.com/10.1029/2005GL025489`

Blewitt, G., 2007: *Treatise on geophysics/Vol. 3.: Geodesy*. Elsevier, 446 pp.

Boebel, O., J. R. E. Lutjeharms, C. Schmid, W. Zenk, T. Rossby, and C. Barron, 2003: The Cape Cauldron: a regime of turbulent inter-ocean exchange. *Deep Sea Research Part II: Topical Studies in Oceanography*, **50**, 57–86, doi:10.1016/S0967-0645(02)00379-X.
URL `http://linkinghub.elsevier.com/retrieve/pii/S096706450200379X`

Brooks, C. F., 1932: Bulletin of the National Research Coucil, Chapter Fourteen OCEANOGRAPHY AND METEOROLOGY. *Physics of the Earth*, **5**, 457.

Bryden, H. L., L. M. Beal, and L. M. Duncan, 2005: Structure and transport of the Agulhas Current and its temporal variability. *Journal of Oceanography*, **61**, 479–492.
URL `http://www.springerlink.com/index/L6880HJ337438QQ7.pdf`

Byrne, D. A. and J. L. McClean, 2008: Sea level anomaly signals in the Agulhas Current region. *Geophysical Research Letters*, **35**, L13601, doi:10.1029/2008GL034087.
URL `http://doi.wiley.com/10.1029/2008GL034087`

Cazenave, A., 2010: Sea-level rise and its impact on coastal zones. *Science*, **328**, 1517, doi:10.1126/science.1185782.
URL `http://www.sciencemag.org/cgi/content/abstract/328/5985/1517`

Cazenave, A., K. Dominh, S. Guinehut, E. Berthier, W. Llovel, G. Ramillien, M. Ablain, and G. Larnicol, 2009: Sea level budget over 2003-2008: A reevaluation from GRACE space gravimetry, satellite altimetry and Argo. *Global and Planetary Change*, **65**, 83–88, doi:10.1016/j.gloplacha.2008.10.004.
URL `http://linkinghub.elsevier.com/retrieve/pii/S0921818108001343`

Chambers, D. P., J. Wahr, and R. S. Nerem, 2004: Preliminary observations of global ocean mass variations with GRACE. *Geophysical Research Letters*, **31**, L13310, doi:10.1029/2004GL020461.
URL `http://www.agu.org/pubs/crossref/2004.../2004GL020461.shtml`

Chambers, D. P. and J. K. Willis, 2010: A Global Evaluation of Ocean Bottom Pressure from GRACE, OMCT, and Steric-Corrected Altimetry. *Journal of Atmospheric and Oceanic Technology*, **27**, 1395–1402, doi:10.1175/2010JTECHO738.1.
URL http://journals.ametsoc.org/doi/abs/10.1175/2010JTECHO738.1

Church, J. A. and N. J. White, 2006: A 20th century acceleration in global sea-level rise. *Geophysical Research Letters*, **33**, L01602, doi:10.1029/2005GL024826.
URL http://www.agu.org/pubs/crossref/2006/2005GL024826.shtml

Crossley, D., C. de Linage, J. Hinderer, J.-P. Boy, and J. Famiglietti, 2012: A comparison of the gravity field over Central Europe from superconducting gravimeters, GRACE and global hydrological models, using EOF analysis. *Geophysical Journal International*, **189**, 877–897, doi:10.1111/j.1365-246X.2012.05404.x.
URL http://dx.doi.org/10.1111/j.1365-246X.2012.05404.x

Dahle, C., F. Flechtner, C. Gruber, D. König, R. König, G. Michalak, and K. H. Neumayer, 2013: GFZ RL05 - an improved time-series of monthly GRACE gravity field solutions. *Geotechnologien Science Report No. 20 "Observation of the System Earth from Space – CHAMP, GRACE, GOCE and future missions"*, Springer, Heidelberg.

Dee, D. P., S. M. Uppala, A. J. Simmons, P. Berrisford, P. Poli, S. Kobayashi, U. Andrae, M. A. Balmaseda, G. Balsamo, P. Bauer, P. Bechtold, A. C. M. Beljaars, L. van de Berg, J. Bidlot, N. Bormann, C. Delsol, R. Dragani, M. Fuentes, A. J. Geer, L. Haimberger, S. B. Healy, H. Hersbach, E. V. Hólm, L. Isaksen, P. Kå llberg, M. Köhler, M. Matricardi, A. P. McNally, B. M. Monge-Sanz, J.-J. Morcrette, B.-K. Park, C. Peubey, P. de Rosnay, C. Tavolato, J.-N. Thépaut, and F. Vitart, 2011: The ERA-Interim reanalysis: configuration and performance of the data assimilation system. *Quarterly Journal of the Royal Meteorological Society*, **137**, 553–597, doi:10.1002/qj.828.
URL http://doi.wiley.com/10.1002/qj.828

Dill, R., 2008: Hydrological model LSDM for operational Earth rotation and gravity field variations - STR 08/09. Technical report, GFZ German Research Centre for Geosciences, Potsdam.

Dobslaw, H., 2007: *Modellierung der allgemeinen ozeanischen Dynamik zur Korrektur und Interpretation von Satellitendaten - STR 07/10*. Ph.D. thesis, GFZ German Research Centre for Geosciences, Potsdam, 113 pp.

Dobslaw, H., R. Dill, A. Grötzsch, A. Brzezinski, and M. Thomas, 2010: Seasonal polar motion excitation from numerical models of atmosphere, ocean, and continental hydrosphere. *Journal of Geophysical Research*, **115**, B10406, doi:10.1029/2009JB007127.
URL http://www.agu.org/pubs/crossref/2010/2009JB007127.shtml

Dobslaw, H., F. Flechtner, I. Bergmann-Wolf, C. Dahle, R. Dill, S. Esselborn, I. Sasgen, and M. Thomas, 2013: Simulating high-frequency atmosphere-ocean mass variability for dealiasing

of satellite gravity observations: AOD1B RL05. *Journal of Geophysical Research: Oceans*, n/a–n/a, doi:10.1002/jgrc.20271.
URL http://doi.wiley.com/10.1002/jgrc.20271

Dobslaw, H. and M. Thomas, 2007: Simulation and observation of global ocean mass anomalies. *Journal of Geophysical Research*, **112**, C05040, doi:10.1029/2006JC004035.
URL http://www.agu.org/journals/ABS/2007/2006JC004035.shtmlhttp://www.agu.org/pubs/crossref/2007/2006JC004035.shtml

Doglioli, A. M., B. Blanke, S. Speich, and G. Lapeyre, 2007: Tracking coherent structures in a regional ocean model with wavelet analysis: Application to Cape Basin eddies. *Journal of Geophysical Research*, **112**, C05043, doi:10.1029/2006JC003952.
URL http://www.agu.org/pubs/crossref/2007/2006JC003952.shtml

Doodson, A. T. and H. D. Warburg, 1941: Admiralty manual of tides. *H.M. Stationery Office*.

Drews, C. and W. Han, 2010: Dynamics of wind setdown at Suez and the Eastern Nile Delta. *PloS one*, **5**, e12481, doi:10.1371/journal.pone.0012481.
URL http://www.pubmedcentral.nih.gov/articlerender.fcgi?artid=2932978&tool=pmcentrez&rendertype=abstract

Drijfhout, S. and C. Heinze, 1996: Mean circulation and internal variability in an ocean primitive equation model. *Journal of Physical Oceanography*, **26**, 559–580.
URL http://eprints.ifm-geomar.de/13046/

Dziewonski, A. M. and D. L. Anderson, 1981: Preliminary reference Earth model. *Physics of the Earth and Planetary Interiors*, **25**, 297–356.
URL http://linkinghub.elsevier.com/retrieve/pii/0031920181900467

Egbert, G. D., A. F. Bennett, and M. G. G. Foreman, 1994: TOPEX/POSEIDON tides estimated using a global inverse model. *Journal of Geophysical Research*, **99**, 24821, doi:10.1029/94JC01894.
URL http://www.agu.org/pubs/crossref/1994/94JC01894.shtml

Farrell, W. E., 1972: Deformation of the Earth by Surface Loads. *Reviews of Geophysics and Space Physics*, **10**, 761–797.

— 1973: Earth Tides, Ocean Tides and Tidal Loading. *Philosophical Transactions of the Royal Society A: Mathematical, Physical and Engineering Sciences*, **274**, 253–259, doi:10.1098/rsta.1973.0050.
URL http://rsta.royalsocietypublishing.org/content/274/1239/253

Farrell, W. E. and J. A. Clark, 1976: On Postglacial Sea Level. *Geophysical Journal of the Royal Astronomical Society*, **46**, 647–667, doi:10.1111/j.1365-246X.1976.tb01252.x.
URL http://doi.wiley.com/10.1111/j.1365-246X.1976.tb01252.x

Flechtner, F., 2007: GFZ Level-2 Processing Standards Document. Technical report, GFZ Potsdam, Potsdam.
URL http://isdc.gfz-potsdam.de/index.php?name=UpDownload&req=getit&lid=401

Flechtner, F. and H. Dobslaw, 2013: GRACE 327-750 (GR-GFZ-AOD-0001) Gravity Recovery and Climate Experiment, AOD1B Product Description Document for Product Release 05, Rev. 4.0. Technical report, GFZ German Research Centre for Geosciences, Potsdam.
URL http://isdc.gfz-potsdam.de/index.php?name=UpDownload&req=getit&lid=619

Froyland, G., C. Horenkamp, V. Rossi, N. Santitissadeekorn, and A. S. Gupta, 2012: Three-dimensional characterization and tracking of an Agulhas Ring. *Ocean Modelling*, **52-53**, 69–75, doi:10.1016/j.ocemod.2012.05.001.
URL http://linkinghub.elsevier.com/retrieve/pii/S1463500312000789

Gordeev, R. G., B. A. Kagan, and E. V. Polyakov, 1977: The Effects of Loading and Self-Attraction on Global Ocean Tides: The Model and the Results of a Numerical Experiment. *Journal of Physical Oceanography*, **7**, 161–170, doi:10.1175/1520-0485(1977)007¡0161:TEOLAS¿2.0.CO;2.
URL http://journals.ametsoc.org/doi/abs/10.1175/1520-0485%281977%29007%3C0161%3ATEOLAS%3E2.0.CO%3B2

Greatbatch, R. J., 1994: A note on the representation of steric sea level in models that conserve volume rather than mass. *Journal of Geophysical Research*, **99**, 12767, doi:10.1029/94JC00847.
URL http://dx.doi.org/10.1029/94JC00847http://www.agu.org/pubs/crossref/1994/94JC00847.shtml

Guo, J. Y., X. J. Duan, and C. K. Shum, 2010: Non-isotropic Gaussian smoothing and leakage reduction for determining mass changes over land and ocean using GRACE data. *Geophysical Journal International*, **181**, 290–302, doi:10.1111/j.1365-246X.2010.04534.x.
URL http://gji.oxfordjournals.org/cgi/doi/10.1111/j.1365-246X.2010.04534.x

Han, S.-C. and P. Ditmar, 2007: Localized spectral analysis of global satellite gravity fields for recovering time-variable mass redistributions. *Journal of Geodesy*, **82**, 423–430, doi:10.1007/s00190-007-0194-5.
URL http://link.springer.com/10.1007/s00190-007-0194-5

Hannachi, A., I. T. Jolliffe, and D. B. Stephenson, 2007: Empirical orthogonal functions and related techniques in atmospheric science : A review. *International Journal of Climatology*, **27**, 1119–1152, doi:10.1002/joc.

Hendershott, M. C., 1972: The Effects of Solid Earth Deformation on Global Ocean Tides. *Geophysical Journal International*, **29**, 389–402, doi:10.1111/j.1365-246X.1972.tb06167.x.
URL http://gji.oxfordjournals.org/cgi/doi/10.1111/j.1365-246X.1972.tb06167.x

Hughes, C. W., M. E. Tamisiea, R. J. Bingham, and J. Williams, 2012: Weighing the ocean: Using a single mooring to measure changes in the mass of the ocean. *Geophysical Research Letters*, **39**, L17602, doi:10.1029/2012GL052935.
URL http://doi.wiley.com/10.1029/2012GL052935

Janjić, T., J. Schröter, R. Savcenko, W. Bosch, A. Albertella, R. Rummel, and O. Klatt, 2012: Impact of combining GRACE and GOCE gravity data on ocean circulation estimates. *Ocean Science*, **8**, 65–79, doi:10.5194/os-8-65-2012.
URL http://www.ocean-sci.net/8/65/2012/

Kendall, R. A., J. X. Mitrovica, and G. A. Milne, 2005: On post-glacial sea level - II. Numerical formulation and comparative results on spherically symmetric models. *Geophysical Journal International*, **161**, 679–706, doi:10.1111/j.1365-246X.2005.02553.x.
URL http://doi.wiley.com/10.1111/j.1365-246X.2005.02553.x

Klemann, V., M. Thomas, and H. Schuh, 2013: Elastic and Viscoelastic Reaction of the Lithosphere to Loads. *Handbook of Geomathematics*, W. Freeden, M. Zuhair Nashed, and T. Sonar, eds., Berlin, Heidelberg.

Klemann, V. and D. Wolf, 2007: Using Fuzzy Logic for the Analysis of Sea-level Indicators with Respect to Glacial-isostatic Adjustment: An Application to the Richmond-Gulf Region, Hudson Bay. *Pure and Applied Geophysics*, **164**, 683–696, doi:10.1007/s00024-007-0191-x.
URL http://link.springer.com/10.1007/s00024-007-0191-x

Kothur, P., M. Sips, A. Unger, J. Kuhlmann, and D. Dransch, 2013: Interactive visual summaries for detection and assessment of spatiotemporal patterns in geospatial time series. *Information Visualization*, doi:10.1177/1473871613481692.
URL http://ivi.sagepub.com/lookup/doi/10.1177/1473871613481692

Kroner, C., M. Thomas, H. Dobslaw, M. Abe, and A. Weise, 2009: Seasonal effects of non-tidal oceanic mass shifts in observations with superconducting gravimeters. *Journal of Geodynamics*, **48**, 354–359, doi:10.1016/j.jog.2009.09.009.
URL http://linkinghub.elsevier.com/retrieve/pii/S0264370709000763

Krug, M. and J. Tournadre, 2012: Satellite observations of an annual cycle in the Agulhas Current. *Geophysical Research Letters*, **39**, L15607, doi:10.1029/2012GL052335.
URL http://www.agu.org/pubs/crossref/2012/2012GL052335.shtml

Kuhlmann, J., H. Dobslaw, and M. Thomas, 2011: Improved modeling of sea level patterns by incorporating self-attraction and loading. *Journal of Geophysical Research*, **116**, C11036, doi:10.1029/2011JC007399.
URL http://www.agu.org/pubs/crossref/2011/2011JC007399.shtml

Kurtenbach, E., T. Mayer-Gürr, and A. Eicker, 2009: Deriving daily snapshots of the Earth's gravity field from GRACE L1B data using Kalman filtering. *Geophysical Research Letters*,

36, L17102, doi:10.1029/2009GL039564.
URL http://www.agu.org/pubs/crossref/2009/2009GL039564.shtml

Kusche, J., R. Schmidt, S. Petrovic, and R. Rietbroek, 2009: Decorrelated GRACE time-variable gravity solutions by GFZ, and their validation using a hydrological model. *Journal of Geodesy*, **83**, 903–913, doi:10.1007/s00190-009-0308-3.
URL http://link.springer.com/10.1007/s00190-009-0308-3

Leuliette, E. W. and L. Miller, 2009: Closing the sea level rise budget with altimetry, Argo, and GRACE. *Geophysical Research Letters*, **36**, L04608, doi:10.1029/2008GL036010.
URL http://www.agu.org/pubs/crossref/2009/2008GL036010.shtml

Lorenz, E. N., 1956: Empirical Orthogonal Functions and Statistical Weather Prediction. *Scientific Report No. 1, Statistical Forecasting Project, MIT, Cambridge, Massachussetts, USA*.

Lutjeharms, J. and D. Webb, 1995: Modelling the Agulhas current system with FRAM (fine resolution antarctic model). *Deep Sea Research Part I: Oceanographic Research Papers*, **42**, 523–551, doi:10.1016/0967-0637(94)00031-M.
URL http://linkinghub.elsevier.com/retrieve/pii/096706379400031M

Lutjeharms, J. R. E., 1981: Spatial scales and intensities of circulation in the ocean areas adjacent to South Africa. *Deep Sea Research Part A. Oceanographic Research Papers*, **28**, 1289–1302, doi:10.1016/0198-0149(81)90035-2.
URL http://linkinghub.elsevier.com/retrieve/pii/0198014981900352

Lutjeharms, J. R. E., R. Catzel, and H. Valentine, 1989: Eddies and other boundary phenomena of the Agulhas Current. *Continental Shelf Research*, **9**, 597–616, doi:10.1016/0278-4343(89)90032-0.
URL http://linkinghub.elsevier.com/retrieve/pii/0278434389900320

Macrander, A., C. Böning, O. Boebel, and J. Schröter, 2010: Validation of GRACE Gravity Fields by In-Situ Data of Ocean Bottom Pressure. *System Earth via Geodetic-Geophysical Space Techniques*, F. M. Flechtner, T. Gruber, A. Güntner, M. Mandea, M. Rothacher, T. Schöne, and J. Wickert, eds., Springer Berlin Heidelberg, Advanced Technologies in Earth Sciences, 169–185.

Meehl, G. A., T. Stocker, W. Collins, P. Friedlingstein, A. Gaye, J. M. Gregory, A. Kitoh, R. Knutti, J. Murphy, A. Noda, S. Raper, I. Watterson, A. Weaver, and Z.-C. Zhao, 2007: Global Climate Projections. *Climate Change 2007: The Physical Science Basis. Contribution of Working Group I to the Fourth Assessment Report of the Intergovernmental Panel on Climate Change*, S. Solomon, D. Qin, M. Manning, Z. Chen, M. Marquis, K. Averyt, M. Tignor, and H. Miller, eds., Cambridge University Press, Cambridge, United Kingdom and New York, NY, USA, chapter 10.
URL http://www.meteosat.com/ipcc4/Ch10_SOD_Text_TSU_FINAL.pdf

Meyssignac, B. and A. Cazenave, 2012: Sea level: A review of present-day and recent-past changes and variability. *Journal of Geodynamics*, **58**, 96–109, doi:10.1016/j.jog.2012.03.005.
URL http://linkinghub.elsevier.com/retrieve/pii/S0264370712000464

Müller, M., 2007: *A large spectrum of free oscillations of the World Ocean including the full ocean loading and self-attraction effects*. Phd thesis, Universität Hamburg, 103 pp.
URL http://www.springerlink.com/content/978-3-540-85575-0

— 2008: Synthesis of forced oscillations, Part I: Tidal dynamics and the influence of the loading and self-attraction effect. *Ocean Modelling*, **20**, 207–222, doi:10.1016/j.ocemod.2007.09.001.
URL http://linkinghub.elsevier.com/retrieve/pii/S1463500307001151

Munk, W., 2002: Twentieth century sea level: An enigma. *Proceedings of the National Academy of Sciences*, **99**, 6550, doi:10.1073/pnas.092704599.
URL http://www.pnas.org/content/99/10/6550.full

Munk, W. and G. J. F. MacDonald, 1960: *The Rotation of the Earth - A Geophysical Discussion*. Cambridge University Press, 323 pp.

Oliver, E. C. J. and K. R. Thompson, 2010: Madden-Julian Oscillation and sea level: Local and remote forcing. *Journal of Geophysical Research*, **115**, C01003, doi:10.1029/2009JC005337.
URL http://www.agu.org/pubs/crossref/2010/2009JC005337.shtml

Penven, P., J. R. E. Lutjeharms, and P. Florenchie, 2006: Madagascar: A pacemaker for the Agulhas Current system? *Geophysical Research Letters*, **33**, L17609, doi:10.1029/2006GL026854.
URL http://www.agu.org/pubs/crossref/2006/2006GL026854.shtml

Penven, P., P. Marchesiello, L. Debreu, and J. Lefèvre, 2008: Software tools for pre- and post-processing of oceanic regional simulations. *Environmental Modelling & Software*, **23**, 660–662, doi:10.1016/j.envsoft.2007.07.004.
URL http://linkinghub.elsevier.com/retrieve/pii/S1364815207001296

Quinn, K. J. and R. M. Ponte, 2011: Estimating high frequency ocean bottom pressure variability. *Geophysical Research Letters*, **38**, 1–5, doi:10.1029/2010GL046537.
URL http://www.agu.org/pubs/crossref/2011/2010GL046537.shtml

Ray, R. D., 1998: Ocean self-attraction and loading in numerical tidal models. *Marine Geodesy*, **21**, 181–192, doi:10.1080/01490419809388134.

Ray, R. D. and D. A. Byrne, 2010: Bottom pressure tides along a line in the southeast Atlantic Ocean and comparisons with satellite altimetry. *Ocean Dynamics*, **60**, 1167–1176, doi:10.1007/s10236-010-0316-0.
URL http://link.springer.com/10.1007/s10236-010-0316-0

Richter, K., R. Riva, and H. Drange, 2013: Impact of self-attraction and loading effects induced by shelf mass loading on projected regional sea level rise. *Geophysical Research Letters*, **40**,

1144–1148, doi:10.1002/grl.50265.
URL http://doi.wiley.com/10.1002/grl.50265

Rietbroek, R., P. LeGrand, B. Wouters, J.-M. Lemoine, G. Ramillien, and C. W. Hughes, 2006: Comparison of in situ bottom pressure data with GRACE gravimetry in the Crozet-Kerguelen region. *Geophysical Research Letters*, **33**, L21601, doi:10.1029/2006GL027452.
URL http://doi.wiley.com/10.1029/2006GL027452

Rouault, M., P. Penven, and B. Pohl, 2009: Warming in the Agulhas Current system since the 1980's. *Geophysical Research Letters*, **36**, L12602, doi:10.1029/2009GL037987.
URL http://www.agu.org/pubs/crossref/2009/2009GL037987.shtml

Rummel, R., W. Yi, and C. Stummer, 2011: GOCE gravitational gradiometry. *Journal of Geodesy*, **85**, 777–790, doi:10.1007/s00190-011-0500-0.
URL http://link.springer.com/10.1007/s00190-011-0500-0

Sasgen, I., Z. Martinec, and K. Fleming, 2007: Regional ice-mass changes and glacial-isostatic adjustment in Antarctica from GRACE. *Earth and Planetary Science Letters*, **264**, 391–401, doi:10.1016/j.epsl.2007.09.029.
URL http://linkinghub.elsevier.com/retrieve/pii/S0012821X07005961

Schmidt, R., P. Schwintzer, F. Flechtner, C. Reigber, a. Guntner, P. Doll, G. Ramillien, a. Cazenave, S. Petrovic, and H. Jochmann, 2006: GRACE observations of changes in continental water storage. *Global and Planetary Change*, **50**, 112–126, doi:10.1016/j.gloplacha.2004.11.018.
URL http://linkinghub.elsevier.com/retrieve/pii/S0921818105000317

Schouten, M. W., W. P. de Ruijter, P. J. van Leeuwen, and H. Ridderinkhof, 2003: Eddies and variability in the Mozambique Channel. *Deep Sea Research Part II: Topical Studies in Oceanography*, **50**, 1987–2003, doi:10.1016/S0967-0645(03)00042-0.
URL http://linkinghub.elsevier.com/retrieve/pii/S0967064503000420

Schouten, M. W., W. P. M. de Ruijter, P. J. van Leeuwen, and J. R. E. Lutjeharms, 2000: Translation, decay and splitting of Agulhas rings in the southeastern Atlantic Ocean. *Journal of Geophysical Research*, **105**, 21913, doi:10.1029/1999JC000046.
URL http://onlinelibrary.wiley.com/doi/10.1029/1999JC000046/fullhttp://doi.wiley.com/10.1029/1999JC000046

Shchepetkin, A. F. and J. C. McWilliams, 2005: The regional oceanic modeling system (ROMS): a split-explicit, free-surface, topography-following-coordinate oceanic model. *Ocean Modelling*, **9**, 347–404, doi:10.1016/j.ocemod.2004.08.002.
URL http://linkinghub.elsevier.com/retrieve/pii/S1463500304000484

Smagorinsky, J., 1963: General Circulation Experimentes With The Primitive Equations. *Monthly Weather Review*, **91**, 99–164, doi:10.1175/1520-0493(1963)091¡0099:GCEWTP¿2.3.CO;2.

URL http://journals.ametsoc.org/doi/abs/10.1175/1520-0493%281963%29091%3C0099%3AGCEWTP%3E2.3.CO%3B2

Smirnow, W. I., 1955: *Lehrgang der Höheren Mathematik Teil III,2*. VEB Deutscher Verlag der Wissenschaften, Berlin, 601 pp.

Smith, T. M., R. W. Reynolds, R. E. Livezey, and D. C. Stokes, 1996: Reconstruction of Historical Sea Surface Temperatures Using Empirical Orthogonal Functions. *Journal of Climate*, **9**, 1403–1420, doi:10.1175/1520-0442(1996)009¡1403:ROHSST¿2.0.CO;2.
URL http://journals.ametsoc.org/doi/abs/10.1175/1520-0442%281996%29009%3C1403%3AROHSST%3E2.0.CO%3B2

Song, Y. T. and F. Colberg, 2011: Deep ocean warming assessed from altimeters, Gravity Recovery and Climate Experiment, in situ measurements, and a non-Boussinesq ocean general circulation model. *Journal of Geophysical Research*, **116**, C02020, doi:10.1029/2010JC006601.
URL http://www.agu.org/pubs/crossref/2011/2010JC006601.shtml

Stepanov, V. N. and C. W. Hughes, 2004: Parameterization of ocean self-attraction and loading in numerical models of the ocean circulation. *Journal of Geophysical Research*, **109**, C03037, doi:10.1029/2003JC002034.
URL http://www.agu.org/pubs/crossref/2004/2003JC002034.shtml

Tamisiea, M. E., E. M. Hill, R. M. Ponte, J. L. Davis, I. Velicogna, and N. T. Vinogradova, 2010: Impact of self-attraction and loading on the annual cycle in sea level. *Journal of Geophysical Research*, **115**, C07004, doi:10.1029/2009JC005687.
URL http://www.agu.org/pubs/crossref/2010/2009JC005687.shtml

Tapley, B. D., S. Bettadpur, J. C. Ries, P. F. Thompson, and M. M. Watkins, 2004: GRACE measurements of mass variability in the Earth system. *Science*, **305**, 503–5, doi:10.1126/science.1099192.
URL http://www.ncbi.nlm.nih.gov/pubmed/15273390

Taylor, M. H., M. Losch, M. Wenzel, and J. Schröter, 2013: On the sensitivity of field reconstruction and prediction using Empirical Orthogonal Functions derived from gappy data. *Journal of Climate*, 130722130643003, doi:10.1175/JCLI-D-13-00089.1.
URL http://journals.ametsoc.org/doi/abs/10.1175/JCLI-D-13-00089.1

Thomas, M., 2002: *Ozeanisch induzierte Erdrotationsschwankungen: Ergebnisse eines Simultanmodells für Zirkulation und ephemeridische Gezeiten im Weltozean*. Ph.d. thesis, Universität Hamburg, 128 pp.

Thomas, M., J. Sündermann, and E. Maier-Reimer, 2001: Consideration of ocean tides in an OGCM and impacts on subseasonal to decadal polar motion excitation. *Geophysical Research Letters*, **28**, 2457–2460.
URL http://www.agu.org/pubs/crossref/2001.../2000GL012234.shtml

Thompson, K. R. and E. Demirov, 2006: Skewness of sea level variability of the world's oceans. *Journal of Geophysical Research*, **111**, C05005, doi:10.1029/2004JC002839.
URL http://www.agu.org/pubs/crossref/2006/2004JC002839.shtml

Umlauf, L. and H. Burchard, 2003: A generic length-scale equation for geophysical turbulence models. *Journal of Marine Research*, **61**, 235–265, doi:10.1357/002224003322005087.
URL http://www.ingentaselect.com/rpsv/cgi-bin/cgi?ini=xref&body=linker&reqdoi=10.1357/002224003322005087

van Aken, H., A. van Veldhoven, C. Veth, W. P. M. De Ruijter, P. J. van Leeuwen, S. Drijfhout, C. Whittle, and M. Rouault, 2003: Observations of a young Agulhas ring, Astrid, during MARE in March 2000. *Deep Sea Research Part II: Topical Studies in Oceanography*, **50**, 167–195, doi:10.1016/S0967-0645(02)00383-1.
URL http://linkinghub.elsevier.com/retrieve/pii/S0967064502003831

van Dam, T. M., X. Collilieux, J. Wuite, Z. Altamimi, and J. Ray, 2012: Nontidal ocean loading: amplitudes and potential effects in GPS height time series. *Journal of Geodesy*, **86**, 1043–1057, doi:10.1007/s00190-012-0564-5.
URL http://link.springer.com/10.1007/s00190-012-0564-5

van Sebille, E., A. Biastoch, P. J. van Leeuwen, and W. P. M. De Ruijter, 2009: A weaker Agulhas Current leads to more Agulhas leakage. *Geophysical Research Letters*, **36**, 10–13, doi:10.1029/2008GL036614.
URL http://www.agu.org/pubs/crossref/2009/2008GL036614.shtml

van Sebille, E., W. E. Johns, and L. M. Beal, 2012: Does the vorticity flux from Agulhas rings control the zonal pathway of NADW across the South Atlantic? *Journal of Geophysical Research*, **117**, C05037, doi:10.1029/2011JC007684.
URL http://www.agu.org/pubs/crossref/2012/2011JC007684.shtml

Vinogradova, N. T., 2011: Vinogradova's 2011 EGU Presentation. *EGU General Assembly*.

Vinogradova, N. T., R. M. Ponte, M. E. Tamisiea, J. L. Davis, and E. M. Hill, 2010: Effects of self-attraction and loading on annual variations of ocean bottom pressure. *Journal of Geophysical Research*, **115**, C06025, doi:10.1029/2009JC005783.
URL http://www.agu.org/pubs/crossref/2010/2009JC005783.shtml

Vinogradova, N. T., R. M. Ponte, M. E. Tamisiea, K. J. Quinn, E. M. Hill, and J. L. Davis, 2011: Self-attraction and loading effects on ocean mass redistribution at monthly and longer time scales. *Journal of Geophysical Research*, **116**, C08041, doi:10.1029/2011JC007037.
URL http://www.agu.org/pubs/crossref/2011/2011JC007037.shtml

Wahr, J., 2004: Time-variable gravity from GRACE: First results. *Geophysical Research Letters*, **31**, L11501, doi:10.1029/2004GL019779.
URL http://doi.wiley.com/10.1029/2004GL019779

Wahr, J., M. Molenaar, and F. O. Bryan, 1998: Time variability of the Earth's gravity field: Hydrological and oceanic effects and their possible detection using GRACE. *Journal of Geophysical Research*, **103**, 30205, doi:10.1029/98JB02844.
URL http://doi.wiley.com/10.1029/98JB02844

Wieczorek, M. A. and F. J. Simons, 2005: Localized spectral analysis on the sphere. *Geophysical Journal International*, **162**, 655–675, doi:10.1111/j.1365-246X.2005.02687.x.
URL http://onlinelibrary.wiley.com/doi/10.1111/j.1365-246X.2005.02687.x/full

Williams, S. D. P. and N. T. Penna, 2011: Non-tidal ocean loading effects on geodetic GPS heights. *Geophysical Research Letters*, **38**, 3–7, doi:10.1029/2011GL046940.
URL http://www.agu.org/pubs/crossref/2011/2011GL046940.shtml

Wolff, J.-O., E. Maier-Reimer, and S. Legutke, 1996: The Hamburg Ocean Primitive Equation Model. Technical Report 13.
URL http://mms.dkrz.de/pdf/reports/ReportNo.13.pdf

Woodworth, P. L., N. J. White, S. Jevrejeva, S. J. Holgate, J. A. Church, and W. R. Gehrels, 2009: Evidence for the accelerations of sea level on multi-decade and century timescales. *International Journal of Climatology*, **29**, 777–789, doi:10.1002/joc.
URL http://onlinelibrary.wiley.com/doi/10.1002/joc.1771/abstract

Wu, P., 2004: Using commercial finite element packages for the study of earth deformations, sea levels and the state of stress. *Geophysical Journal International*, **158**, 401–408, doi:10.1111/j.1365-246X.2004.02338.x.
URL http://gji.oxfordjournals.org/cgi/doi/10.1111/j.1365-246X.2004.02338.x

Wunsch, C., R. M. Ponte, and P. Heimbach, 2007: Decadal trends in sea level patterns: 1993-2004. *Journal of Climate*, **20**, 5889–5911, doi:10.1175/2007JCLI1840.1.
URL http://journals.ametsoc.org/doi/abs/10.1175/2007JCLI1840.1

Yang, X., D. Venturi, C. Chen, C. Chryssostomidis, and G. E. Karniadakis, 2010: EOF-based constrained sensor placement and field reconstruction from noisy ocean measurements: Application to Nantucket Sound. *Journal of Geophysical Research*, **115**, C12072, doi:10.1029/2010JC006148.
URL http://doi.wiley.com/10.1029/2010JC006148

Yin, J., S. M. Griffies, and R. J. Stouffer, 2010: Spatial Variability of Sea Level Rise in Twenty-First Century Projections. *Journal of Climate*, **23**, 4585–4607, doi:10.1175/2010JCLI3533.1.
URL http://cat.inist.fr/?aModele=afficheN&cpsidt=23203551

Zahel, W., 1991: Modeling ocean tides with and without assimilating data. *Journal of Geophysical Research*, **96**, 20379, doi:10.1029/91JB00424.
URL http://www.agu.org/pubs/crossref/1991/91JB00424.shtml

Acknowledgments/Danksagung

Als Erstes bedanke ich mich bei Maik Thomas dafür, dass seine Tür stets offen stand, um zahllose Fragen zu diskutieren — von den ersten Ergebnisse bis zum Final Draft, von den großen Linien dieser Arbeit bis zur bevorzugten Akronymisierung physikalischer Prozesse. Henryk Dobslaw danke ich für die Begleitung dieser Arbeit in allen Details, für eine noch größere Anzahl an Diskussionen und für seinen kritischen Blick auf jegliche Ungenauigkeiten. Zweifellos am meisten Zeit verbracht habe ich während meiner Promotion mit Christof Petrick, der zwar dreieinhalb Jahre lang den Fensterplatz okkupiert, sich aber immerhin als unterhaltsamer Diskussionspartner, und im Normalfall -gegner, erwiesen hat. Insbesondere Kapitel 6 ist ein Kind dieser Diskussionen. Irina Rogozhina, who still refuses to speak German, will get her acknowledgment in English: Thank you for your ecstatic support, especially during the work on Chapter 8. I apologize for not submitting it to *Nature* after all. Robert Dill danke ich einerseits für die Diskussionen, die zu Kapitel 8 geführt haben; andererseits für seine Gastfreundschaft während der traditionellen Kaffeepausen. Inga Bergmann-Wolf hat viel Arbeit in die Beschaffung, Konvertierung und Nutzbarmachung des größten Teils der in dieser Arbeit benutzten Messdaten gesteckt, wofür ich ihr herzlich danke. Patrick Köthur wiederum danke ich dafür, dass ich mich in der überaus angenehmen und nebenbei auch erfolgreichen Zusammenarbeit mit ihm, und später auch mit Madline Kniebusch, endlich einmal als "Experte" fühlen durfte. Bei Jan Brinkmann und Jan Saynisch bedanke ich mich dafür, dass sie eine frühere Version dieser Arbeit korrigiert und verbessert bzw. auseinandergenommen haben. Ich hoffe, diese Version findet Gnade vor den Augen insbesondere Jan Saynischs, dem ich zudem danke, dass er das ROMS-Setup, in das ich so viel Arbeit investiert habe, nun vor dem Verstauben rettet. Ich danke dem GFZ Potsdam für die Finanzierung des ersten und dem Bundesministerium für Bildung und Forschung für die Finanzierung des letzten Teils meiner Promotion — und Henryk Dobslaw dafür, dass er dem BMBF diese Investition schmackhaft gemacht hat. Dem Deutschen Klimarechenzentrum danke ich für die Bereitstellung und Instandhaltung der Infrastruktur, auf der meine Modelle laufen und meine Daten lagern konnten. Außerdem danke ich dem überraschend stabilen Brett aus Fichtenholz für unverhofften Urlaub und den Doktoranden aus der Sofia für die Gelegenheit zum regelmäßigen Lamentieren. Abschließend bedanke ich mich ganz besonders bei meiner geliebten Frau Gwendolyn Reid Kuhlmann, die immer daran geglaubt hat, dass ich diese Doktorarbeit irgendwann zu einem glücklichen Ende würde bringen können.

Eidesstattliche Erklärung

Hiermit versichere ich, die vorliegende Dissertation selbstständig und ohne unerlaubte Hilfe angefertigt zu haben. Es wurden keine anderen als die im Text aufgeführten Hilfsmittel und Quellen verwendet. Ein Promotionsverfahren wurde zu keinem früheren Zeitpunkt an einer anderen Hochschule oder bei einem anderen Fachbereich beantragt.

Julian Kuhlmann
Berlin, Oktober 2013